Myosin dilated cardiomyopathy mutation S532P disrupts actomyosin interactions, leading to altered muscle kinetics, reduced locomotion, and cardiac dilation in *Drosophila*

Adriana S. Trujillo[a], Karen H. Hsu[a], Joy Puthawala[b], Meera C. Viswanathan[c], Amy Loya[b], Thomas C. Irving[d], Anthony Cammarato[c], Douglas M. Swank[b], and Sanford I. Bernstein[a,*]

[a]Department of Biology, Molecular Biology Institute, Heart Institute, San Diego State University, San Diego, CA 92182; [b]Department of Biological Sciences and Center for Biotechnology and Interdisciplinary Studies, Rensselaer Polytechnic Institute, Troy, NY 12180; [c]Division of Cardiology, Department of Medicine, Johns Hopkins University, Baltimore, MD 21205; [d]Center for Synchrotron Radiation Research and Instrumentation and Department of Biological Sciences, Illinois Institute of Technology, Chicago, IL 60616

ABSTRACT **Dilated cardiomyopathy (DCM), a life-threatening disease characterized by pathological heart enlargement, can be caused by myosin mutations that reduce contractile function. To better define the mechanistic basis of this disease, we employed the powerful genetic and integrative approaches available in *Drosophila melanogaster*. To this end, we generated and analyzed the first fly model of human myosin–induced DCM. The model reproduces the S532P human β-cardiac myosin heavy chain DCM mutation, which is located within an actin-binding region of the motor domain. In concordance with the mutation's location at the actomyosin interface, steady-state ATPase and muscle mechanics experiments revealed that the S532P mutation reduces the rates of actin-dependent ATPase activity and actin binding and increases the rate of actin detachment. The depressed function of this myosin form reduces the number of cross-bridges during active wing beating, the power output of indirect flight muscles, and flight ability. Further, *S532P* mutant hearts exhibit cardiac dilation that is mutant gene dose–dependent. Our study shows that *Drosophila* can faithfully model various aspects of human DCM phenotypes and suggests that impaired actomyosin interactions in S532P myosin induce contractile deficits that trigger the disease.**

Monitoring Editor
Dennis Discher
University of Pennsylvania

Received: Feb 26, 2021
Revised: May 27, 2021
Accepted: May 28, 2021

INTRODUCTION

Dilated cardiomyopathy (DCM) involves weakening of the heart, leading to progressive, pathological ventricular dilation and wall thinning (McNally *et al.*, 2013). Hereditary DCM commonly involves point mutations in genes essential for heart function, including the *MYH7* gene encoding human β-cardiac myosin heavy chain (β-MyHC) (Seidman and Seidman, 2001). *MYH7* DCM mutations often disrupt intramolecular and intermolecular interactions essential for proper protein function and decrease contractility (Kamisago *et al.*, 2000; Ujfalusi *et al.*, 2018). Distinct step(s) of the myosin ATPase cycle can be altered by different DCM mutations, depending on the mutation location within the protein and the nature of the amino acid change (Seidman and Seidman, 2001; Richard *et al.*, 2006; Lakdawala *et al.*, 2012; Ujfalusi *et al.*, 2018).

DCM patients exhibit cardiac chamber enlargement with frequent decreases in systolic function and thinning of cardiac walls (Kamisago *et al.*, 2000; Richard *et al.*, 2006). Systolic dysfunction involves inadequate emptying of the left ventricle (LV) that is characterized by reductions in ejection fraction (EF, forward stroke volume divided by end-diastolic volume) and fractional shortening (FS, the

This article was published online ahead of print in MBoC in Press (http://www.molbiolcell.org/cgi/doi/10.1091/mbc.E21-02-0088) on June 3, 2021.

*Address correspondence to: Sanford I. Bernstein (sbernstein@mail.sdsu.edu).

Abbreviations used: α-MyHC, α-cardiac myosin heavy chain; β-MyHC, β-cardiac myosin heavy chain; DCM, dilated cardiomyopathy; DD, diastolic diameter; Ev, viscous modulus; FS, fractional shortening; IFMs, indirect flight muscles; LV, left ventricle; MHC, myosin heavy chain; SD, systolic diameter; S1, myosin subfragment-1; sS1, myosin short subfragment-1.

fraction of diastolic dimension lost during systole). Cardiac dysfunction may be moderate to severe, and histological findings can include fibrosis or cardiomyocyte loss.

In this report, we generate the first *Drosophila* model for myosin-induced DCM (S532P) observed in patients and focus on how this new model could aid in understanding disease causation. In contrast to vertebrates, which contain multigene myosin families, *Drosophila* has a single-copy myosin heavy chain (*Mhc*) gene, making it a simple model to study myosin-based myopathies (Bernstein *et al.*, 1983; Rozek and Davidson, 1983). Further, *Drosophila* serves as an excellent model for the expression and isolation of myosin from indirect flight muscles (IFMs) of the thorax for biochemical and structural studies (Caldwell *et al.*, 2012). Additionally, IFMs contain a highly ordered array of myofibrils similar to human skeletal muscles, and their functional impairment can be readily assessed in vivo by flight testing (Bernstein *et al.*, 1993) and in vitro via fiber mechanical assays (Swank, 2012). *Drosophila* is useful for studying heart disease because many genes controlling heart differentiation and function (e.g., the differentiation factor Tinman/Nkx 2.5, the contractile protein myosin) are evolutionarily conserved (Bier and Bodmer, 2004). The dorsal vessel in *Drosophila* includes the heart, which is composed of a simple tube-like structure located in the abdomen that is part of an open circulatory system. *Drosophila* heart function can be severely perturbed without compromising viability, because flies also utilize a tracheal respiration system to deliver oxygen directly to tissues.

Multiple human patients and a mouse model have confirmed that the S532P mutation is causative of DCM in mammals (Kamisago *et al.*, 2000; Schmitt *et al.*, 2006; Lakdawala *et al.*, 2012). The well-documented nature of this DCM mutation made it ideal both for determining whether the *Drosophila* system can adequately model aspects of human DCM and for applying the integrative approach available in *Drosophila* in order to gain an in-depth understanding of the mechanistic underpinning of the disease.

Here, we expressed the S532P mutation in *Drosophila* to define the mechanistic basis of disease. Mutant myosin was purified from IFMs for actin cosedimentation and ATPase experiments to determine the biochemical mechanisms whereby the mutation reduces myosin function. Skinned fiber mechanics were performed on IFMs to explore the effects of the mutation on power output, ATP affinity, and the rate constants associated with actin binding. Further, we determined the impacts of the mutation on cardiac physiology, whole organism locomotion, and the myofibrillar ultrastructure of cardiac and skeletal muscles, providing an integrative analysis of DCM myosin. Overall, this study highlights the usefulness of the *Drosophila* model system for investigating the effects of specific myosin DCM mutations and for potential testing of therapeutic modalities.

RESULTS

The S532P myosin mutation reduces actin-activated ATPase activity

To predict the structural effects of the S532P mutation, we modeled the location of the conserved S532 residue (Figure 1A, green residue, boxed inset) on the crystal structure of chicken skeletal muscle myosin II in the postrigor configuration (Rayment *et al.*, 1993). We chose this structure for modeling due to its well-documented binding sites for actin (Rayment *et al.*, 1993; Holmes *et al.*, 2004; Koppole *et al.*, 2007; Lorenz and Holmes, 2010). However, we verified the presence of structurally conserved regions containing the residue of interest in the human β-cardiac myosin heavy chain isoform (β-MyHC, PDB ID#: 4DB1) and *Drosophila* embryonic MHC isoform (PDB ID#: 5W1A) crystal structures. The β-MyHC S532 residue (*Drosophila melanogaster* MHC S531) is located within an actin-binding site (red) in a helix-loop-helix motif of the lower 50-kDa subdomain (Rayment *et al.*, 1993). Kamisago *et al.* (2000) predicted that the S532P mutation breaks the α-helical structure and disrupts actomyosin interactions.

To examine the impact of the S532P mutation on myosin biochemical properties, IFM ultrastructure, IFM mechanical properties, and flight ability, we crossed the myosin transgene into an Mhc^{10} myosin-null genetic background. Mhc^{10} flies lack endogenous MHC protein expression in IFMs and jump muscles due to a mutation of an exon splice junction that is specifically utilized in those muscles (Collier *et al.*, 1990). All other muscle types retain expression of the wild-type *Mhc* gene, which obviates embryonic lethality that arises when *Mhc* expression is eliminated in all muscles (O'Donnell and Bernstein, 1988).

To determine the impact of the S532P mutation on the enzymatic activity of myosin, we assessed steady-state ATPase parameters of myosin obtained from dissected IFMs of homozygous fly lines harboring the S532P myosin mutation. An SDS–PAGE analysis of the upper thoraces of young mutant flies confirmed that these lines express wild-type ratios of myosin to actin (Table 1). Both basal Mg-ATPase (0.22 ± 0.08 vs. 0.28 ± 0.11 s^{-1}, $p = 0.32$) and Ca-ATPase (10.81 ± 6.38 vs.15.77 ± 3.33 s^{-1}, $p = 0.16$) did not significantly differ for S532P myosin compared with wild-type myosin (Figure 1B and Supplemental Table S1). We measured Mg-ATPase activity in the presence of increasing concentrations of F-actin to determine whether the S532P mutation affects actin-dependent activity. The V_{max} (maximum ATPase rate) of actin stimulation was reduced approximately threefold for S532P relative to wild-type myosin (0.59 ± 0.28 vs. 1.86 ± 0.49 s^{-1}, $p < 0.001$; Figure 1C and Supplemental Table S1). The K_m value, the actin concentration required to reach 50% V_{max}, did not differ relative to wild type (Supplemental Table S1).

We performed cosedimentation assays to estimate the binding affinity of S532P S1 for F-actin in the rigor state (in the absence of nucleotide). For this, we generated fly lines expressing His-tagged myosin, isolated His-tagged protein from bulk fly homogenates via Ni column chromatography, and then purified the subfragment-1 (S1) motor domain following limited proteolysis. We produced binding curves by incubating increasing amounts of F-actin with fixed amounts of control or mutant S1. Following centrifugation, a majority of S1 remained soluble in actin-free S1 controls, while F-actin was insoluble in S1-free actin controls (Figure 1D). We scanned electrophoretic gels of centrifuged samples and fitted the densities of S1-bound fractions to a hyperbolic function to determine binding affinity (K_d) for F-actin (Figure 1E). The binding affinities (K_d values) for F-actin did not differ statistically between recombinant mutant and control S1 (2003 ± 1040 nM vs. 1260 ± 963 nM, $p = 0.42$). However, the average K_d value for the S532P mutant S1 was ~1.6-fold higher relative to control S1, indicating a trend toward lower actin affinity in this mutant. The K_d values for both mutant and control myosins were ~10-fold higher compared with previously published values for IFI (Miller *et al.*, 2003). The lower affinity reported here may be attributed to a higher concentration of NaCl in the reaction buffer (100 vs. 30 mM), which was adjusted to improve myosin S1 solubility and to better differentiate between mutant and wild-type affinities, which are extremely high at lower salt concentrations (Miller *et al.*, 2003). Though cosedimentation is a standard approach for measuring actin-binding affinity, it is challenging to obtain accurate K_d measurements using this method due to the irreversible binding of actomyosin during sedimentation. Thus, we also performed muscle mechanics (see below) to determine whether the mutation affects actin-binding rates.

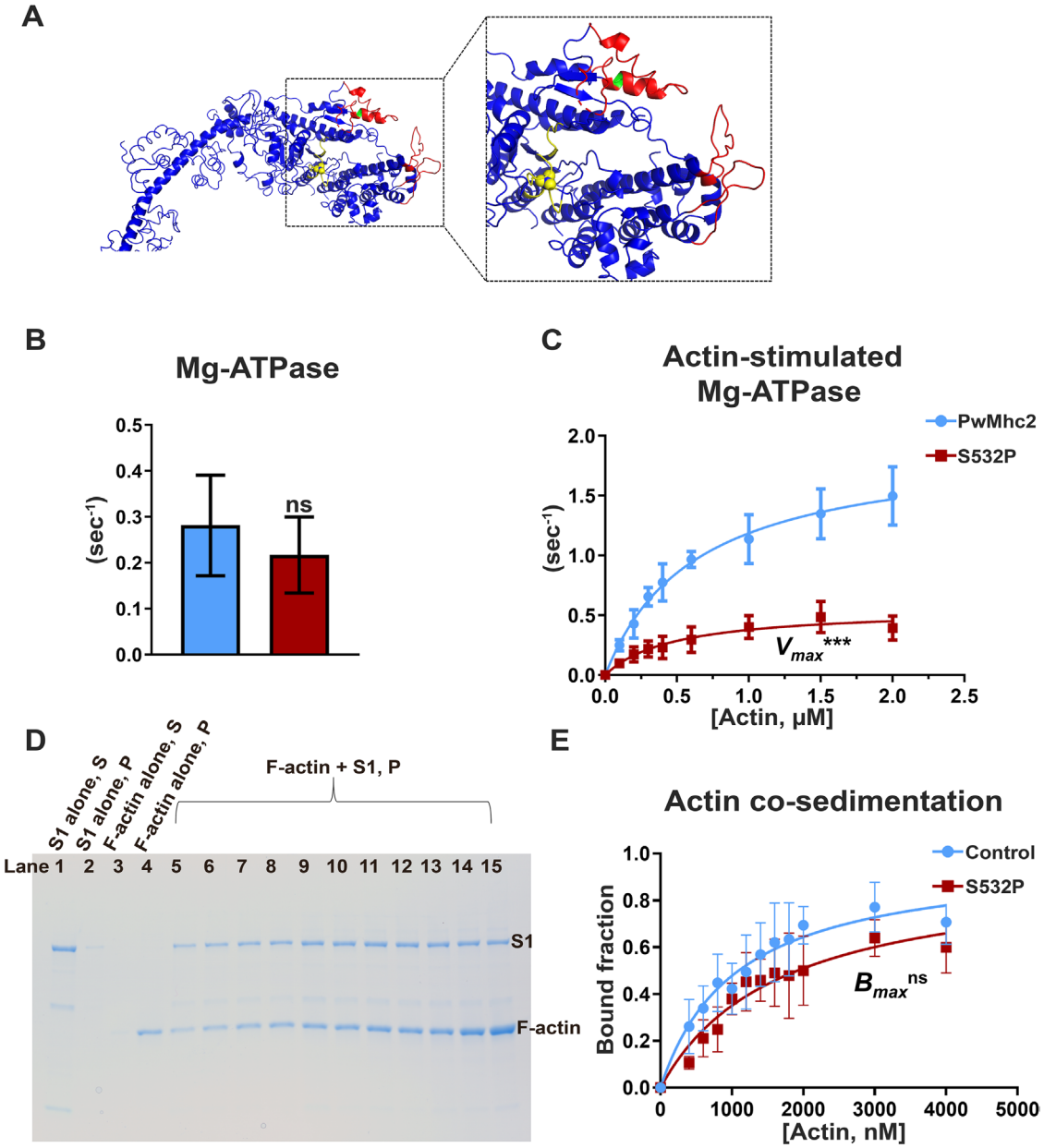

FIGURE 1: S532P myosin reduces steady-state actin-activated ATPase activity. (A) The location of the S532P myosin residue within an actin-binding region of the motor domain is shown in the boxed inset. The β-MyHC S532 residue (green) was modeled on the crystal structure of chicken skeletal muscle myosin II in the postrigor configuration (PDB ID: 2MYS). Red: actin-binding sites. (B, C) Full-length myosin isolated from IFMs of *S532P* mutants ($N = 5$) and *PwMhc2* wild-type transgenic controls ($N = 5$) was assessed for (B) Mg^{2+} basal and (C) actin-activated ATPase activities. To determine actin-activated activity, Mg^{2+} basal ATPase activities were subtracted from measured basal ATPase values over increasing concentrations of F-actin. Values were fitted with the Michaelis–Menten equation to determine the V_{max} and K_m. (D, E) Myosin subfragment-1 (S1) was isolated in bulk from His-tagged *S532P* mutants ($N = 3$) and His-tagged wild-type transgenic controls ($N = 3$) and assessed for actin-binding affinity using cosedimentation assays. (D) A representative SDS–polyacrylamide gel showing insoluble pellet (P) fractions of F-actin and wild-type S1-containing samples over increasing F-actin concentrations (lanes 5–15: 0.4, 0.6. 0.8, 1, 1.2, 1.4, 1.6, 1.8, 2, 3, and 4 μM, respectively). Supernatant (S) and pellet (P) fractions of samples containing S1 or F-actin alone are shown as controls (lanes 1–4). (E) The bound actomyosin levels in pelleted samples were determined via densitometry and plotted vs. F-actin concentration. To determine bound fractions, the density of S1 in the pellet fraction relative to total protein content was calculated, and the fraction of pelleted S1 in a S1-only control was subtracted from this value. To determine actin-binding affinity, the dissociation constant of S1 for F-actin (K_d) was defined as the F-actin concentration required to reach half maximal binding (B_{max}). Data are reported as mean ± SD. Statistical significance was determined using Student's *t* tests (***$p < 0.001$, ns = nonsignificant).

Age	Genotype	Protein expression (%)	Flight index (A.U.)		
		2 d	2 d	1 wk	3 wk
	PwMhc2	100.0 ± 4.7[x]	3.70 ± 0.15	3.52 ± 0.12	3.32 ± 0.13
	S532P-L1	100.6 ± 3.8	3.53 ± 0.21[ns]	1.94 ± 0.16****	1.42 ± 0.17****
	S532P-L2	101.5 ± 1.3	2.70 ± 0.16****	1.75 ± 0.16****	1.76 ± 0.14****
	S532P-L3	99.0 ± 2.2	3.42 ± 0.13[ns]	2.48 ± 0.12****	1.84 ± 0.12****

Homozygous *S532P* mutant lines (*L1*, *L2*, and *L3*) were crossed into an Mhc^{10} (myosin-null in IFMs and jump muscles) background. Protein expression levels in IFMs from *S532P* lines (*L1*, *L2*, and *L3*) relative to wild-type *yw* flies were determined using densitometry. [x]Value given here is for *yw* wild-type flies. *PwMhc2* controls were previously reported to contain wild-type MHC levels relative to those of wild-type flies (Viswanathan *et al.*, 2017). Transgenic flies were assigned a score for flight upward (U), horizontally (H), downward (D) or the inability to fly (N). Flight index was calculated as 6*U/*T* +4*H/*T* +2*D/*T* +0*N/*T*, where *T* is the total number of flies tested. $N \geq 100$ flies were tested for each line/age. Data are reported as mean ± SEM. A two-way ANOVA was employed to test whether the effects of genotype and age were significant for flight indices (Age: $p < 0.0001$, Genotype: $p < 0.0001$, Interaction: $p < 0.0001$). Multiple comparisons between mutant lines and age-matched controls are also shown (****$p < 0.0001$, ns = nonsignificant). Full genotypes of homozygotes are shown in parentheses: *S532P* lines (Mhc^{10}/Mhc^{10}; *P[S532P]/P[S532P]*); *PwMhc2* transgenic controls (*P[PwMhc2]/P[PwMhc2]*; Mhc^{10}/Mhc^{10}).

TABLE 1: Protein expression levels and flight abilities of S532P/S532P lines.

The S532P mutation reduces power output, slows muscle kinetics, and reduces the number of active cross-bridges without affecting myofibril assembly or maintenance

To determine whether expression of the S532P mutation causes defects in myofibrillar assembly or maintenance, we performed transmission electron microscopy on relaxed IFMs isolated from aged 3-wk-old *S532P* homozygous mutants and controls. Transverse sections of mutants and controls displayed myofibrils with normal, rounded morphology (Figure 2, A and B), and a normal double hexagonal array of thick and thin filaments (Figure 2, C and D). In longitudinal sections, myofibrils displayed normal parallel organization (Figure 2, E and F), and sarcomeres displayed normal organization with intact myofilaments (Figure 2, G and H). No differences in average inter–thick filament spacing distances (Figure 2I) or sarcomere lengths (Figure 2J) were detected between mutants and controls under relaxing conditions. Overall, no disruption in sarcomere ultrastructure was observed in *S532P* mutants, suggesting that flight impairment and muscle mechanical changes in these lines (as shown below) were not caused by myofibrillar assembly defects or degeneration.

We performed sinusoidal analysis to determine whether muscle mechanical properties were altered by the S532P mutation. For this, we isolated individual fibers from IFMs of 2–3-d-old homozygous flies, demembranated them, and subjected them to small-amplitude sinusoidal analysis in a muscle mechanics apparatus (Swank, 2012). From the amplitude and phase differences between recorded sinusoidal muscle force and length traces, we calculated mechanical properties such as power, stiffness (elastic and viscous moduli), and rate constants of the myosin cross-bridge cycle. To ensure reproducibility, we assessed fibers isolated from multiple mutant fly lines (*L1*, *L2*, and *L3*).

Fibers from all three mutant homozygous lines displayed depressed maximum power production ($p < 0.05$, one-way variance [ANOVA] Dunn's method) (Table 2 and Figure 3A). The lower power was due, in part, to lower work production as shown by the viscous modulus (Ev) being less negative at frequencies that produced positive power for fibers from *S532P* lines *L2* and *L3* ($p < 0.05$, one-way ANOVA Dunn's method) (Table 2 and Figure 3B). The elastic modulus (in-phase stiffness, Ee) at low and high frequencies was not different from control values, and while intermediate values (at or near f_{max}) are close to being statistically different from control values, differences did not reach statistical significance (Table 2 and Figure 3C). Power was also lower due to slower muscle kinetics (power = work × frequency of muscle oscillation) as shown by the lower frequency at which maximum power was produced, f_{max} ($p < 0.001$, one-way ANOVA Holm–Sidak method) (Table 2 and Figure 3A), the reduced frequency at which the elastic modulus was lowest (fEe or dip frequency) (Table 2 and Figure 3C) and the lower frequency at which the viscous modulus was most negative (fEv or dip frequency) ($p < 0.001$, one-way ANOVA Holm–Sidak method) (Table 2 and Figure 3B) for the mutant. In other words, muscle expressing the mutation operates at slower speeds.

Fitting the Nyquist plots (viscous modulus vs. elastic modulus) (Figure 3E) from sinusoidal analysis with our complex modulus equation (Supplemental Figure S1, Eq. 3) to obtain apparent muscle rate constants $2\pi b$ and $2\pi c$ revealed that the changes in muscle kinetics are likely driven by alterations to some steps of the myosin cross-bridge cycle (Kawai and Brandt, 1980; Swank, 2012). The rate constant $2\pi b$, which is influenced by steps associated with attachment to actin and/or the power stroke step (Palmer, 2010), was significantly slower for fibers from all three mutant lines compared with the controls (Table 2, $p < 0.05$, one-way ANOVA Dunn's method). The rate constant $2\pi c$, which is influenced by steps associated with detachment from actin (Palmer *et al.*, 2007), was significantly faster for fibers from all three mutant lines compared with controls (Table 2, $p < 0.001$, one-way ANOVA Holm–Sidak method). Taken together, the two experimental rate constants suggest that the mutant myosin spends less time strongly bound to actin than the control, which would contribute to the lower work production.

Though the rate of Mg-ADP release is thought to be the rate-limiting step for detachment for most muscle types (Kawai and Halvorson, 1989, 1991), including *Drosophila* embryonic myosin and other slow *Drosophila* muscles (Swank *et al.*, 2006), the ATP-induced detachment step has been identified as rate limiting for *Drosophila* IFMs (Swank *et al.*, 2006). To determine whether the S532P mutation influences the detachment-associated steps, we varied ATP concentration from 20 to 0.5 mM while performing a sinusoidal analysis. We plotted values for f_{max} over changing ATP concentration and fitted them with a hyperbolic function curve (Table 2 and Figure 3D). V_{max} was significantly lower for *S532P* mutant fibers ($p < 0.001$, one-way ANOVA Holm–Sidak method), confirming our previous f_{max} differences, but there was no change in K_m, indicating that the affinity for ATP was not likely changed by the mutation. This suggests that another step associated with myosin detachment from actin, such as ADP release rate, is likely increased to account for the increase in $2\pi c$.

To examine the structural effects of the S532P mutation in vivo, we compared the x-ray diffraction patterns obtained from mutant

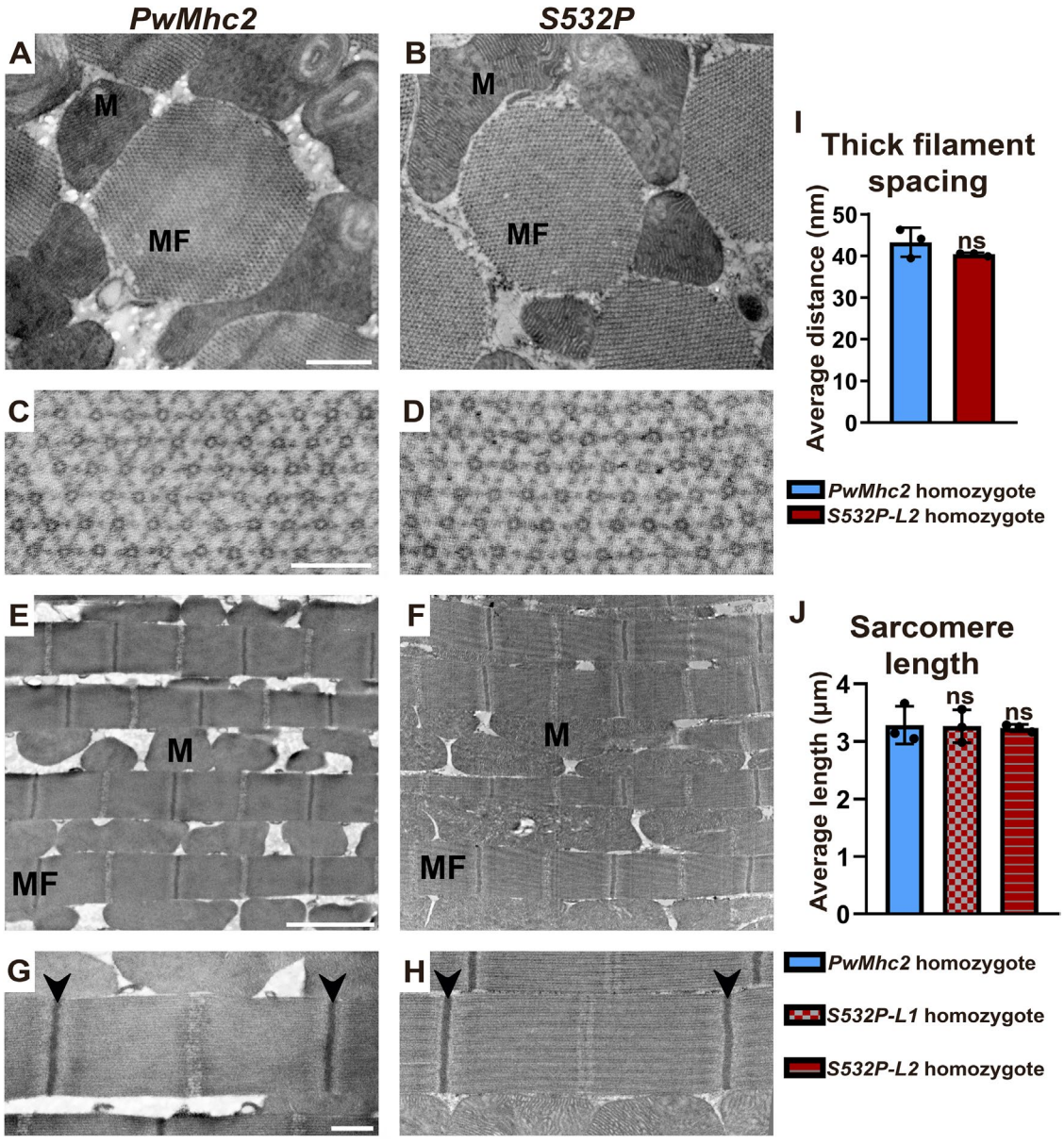

FIGURE 2: The S532P mutation does not affect myofibril stability of *S532P* IFMs. Transmission electron micrographs of thin-sectioned IFMs in transverse and longitudinal orientations were obtained from 3-wk-old homozygous *PwMhc2* control or *S532P* mutant flies in a homozygous Mhc^{10} (myosin-null in IFMs and jump muscles) background. (A, B) Low-magnification images of transverse sections show that myofibrillar morphology of IFMs is normal in *S532P* mutant flies compared with controls. MF: myofibril, M: mitochondrion. Scale bar, 0.5 µm. (C, D) High-magnification images of transverse sections show a regular hexagonal array of thick and thin filaments in controls and mutants. Scale bar, 0.1 µm. (E, F) Low-magnification images of myofibrils from longitudinal sections show that myofibrillar organization is normal in *S532P* flies compared with controls. MF: myofibril, M: mitochondrion. Scale bar, 2 µm. (G, H) High-magnification images of longitudinal sections show that sarcomere stability is maintained in mutants. Arrowheads: Z-disks. Scale bar, 0.5 µm. (I) Inter–thick filament spacing averages were determined from micrographs of transverse sections using a custom-written Python script. Three flies were tested for each line. (J) Average sarcomere lengths were determined from micrographs of longitudinal sections using ImageJ software. Three flies were tested for each line. Values represent mean ± SD. Statistical significance was determined using Student's *t* tests, where ns = nonsignificant difference compared with controls. Full genotypes are shown in parentheses: *S532P* homozygote (Mhc^{10}/Mhc^{10}; *P[S532P]/P[S532P]*); *PwMhc2* homozygote (*P[PwMhc2]/P[PwMhc2]*; Mhc^{10}/Mhc^{10}).

and control IFMs during active contraction (Figure 4A). Figure 4B shows equatorial x-ray diffraction patterns (top) and the intensity traces along the equator out to the 2,0 reflection (bottom) from transgenic wild-type IFM. We used equatorial reflection intensity traces to determine the differences in the intensity of the individual equatorial reflections between IFMs of mutant and control lines. Lattice spacing of active S532P fibers (Figure 4C) is reduced by about 4.1 nm compared with transgenic wild-type fibers (mean ± SEM, 43.61 ± 0.81 vs. 47.76 ± 0.11 nm, $p < 0.0001$). The ratio of 1,0 and 2,0 intensity ($I_{2,0}/I_{1,0}$) is an estimate of shifts of molecular mass from

Genotype	Max power (W/m^3)	f_{max} (Hz)	Elastic modulus (Ee) at max power (kN/m^2)	Dip frequency (fEe) (Hz)	Viscous modulus (Ev) at max power (kN/m^2)	Dip frequency (fEv) (Hz)	$2\pi b$ (s^{-1})	$2\pi c$ (s^{-1})	V_{max} (s^{-1})	K_m (mM)
PwMhc2	164 ± 15	191 ± 5	309 ± 28	293 ± 4	−189 ± 19	166 ± 5	1680.8 ± 74.4	2845.0 ± 122.6	243.9 ± 7.5	3.0 ± 0.6
S532P-L1	86 ± 20*	148 ± 4***	419 ± 83	272 ± 5*	−125 ± 32	114 ± 4***	945.6 ± 39.6*	6046.0 ± 506.0***	173.6 ± 3.1***	1.7 ± 0.2
S532P-L2	63 ± 6*	131 ± 4***	368 ± 20	251 ± 8*	−108 ± 12*	103 ± 3***	766.6 ± 25.7*	6660.2 ± 650.32***	162 ± 5.4***	2.2 ± 0.5
S532P-L3	71 ± 16*	143 ± 4***	401 ± 67	282 ± 23	−126 ± 24*	113 ± 4***	878.9 ± 42.3*	6321.7 ± 582***	172.5 ± 10.2***	1.8 ± 0.1

Sinusoidal analysis was performed on homozygous *PwMhc2* ($N = 10$), *S532P-L1* ($N = 8$), *S532P-L2* ($N = 6$), and *S532P-L3* ($N = 8$) IFM fibers. Maximum power output and the frequency at which maximum power is generated (f_{max}) are shown. Elastic modulus (Ee) and viscous modulus (Ev) values were measured at the oscillation frequency that produced the maximum power value for each fiber. The complex modulus was fitted to a three-term equation (Supplemental Figure S1, Eq. 3) to determine exponential rate processes. Frequencies b and c were multiplied by 2π to convert from frequency to time (s^{-1}), to determine rate constants associated with work-producing ($2\pi b$) and work-absorbing ($2\pi c$) steps of the cross-bridge cycle. Sinusoidal analysis was performed with varied [ATP] to determine ATP affinity. Values for f_{max} were plotted over changing [ATP] and fitted with a hyperbolic function curve to determine V_{max} and K_m. Data are reported as mean ± SEM. One-way ANOVAs were performed to determine statistical significance (***$p < 0.001$, Holm–Sidak method; *$p < 0.05$, Dunn's method). Full genotypes of homozygotes are shown in parentheses: *S532P* lines (Mhc^{10}/Mhc^{10}; *P[S532P1]/P[S532P1]*); *PwMhc2* transgenic controls (*P[PwMhc2]/P[PwMhc2]*; Mhc^{10}/Mhc^{10}).

TABLE 2: Small-amplitude sinusoidal analysis parameters for S532P fibers.

the region of the thick filament to that of the thin filament. Figure 4D shows that the $I_{2,0}/I_{1,0}$ of S532P was significantly decreased relative to that of transgenic wild-type flies (0.623 ± 0.072 vs. 0.852 ± 0.037, $p < 0.01$), suggesting that S532P myosin heads are less associated with the thin filament and fewer cross-bridges are formed during active contraction compared with controls. This agrees with our muscle mechanics results, which suggest that the mutation decreases the number of cross-bridges bound.

The S532P mutation causes a progressive decline in locomotion in *Drosophila*

We compared flight abilities between mutant lines and *PwMhc2* (*P* element-transformed wild type) controls to determine whether the S532P mutation affects animal locomotion (Table 1 and Supplemental Table S2). At 2 d of age, homozygous S532P lines *L1* and *L3* showed no significant difference in flight ability relative to controls (Table 1). Homozygous line *S532P-L2* showed reduced flight ability at this age compared with controls. All three lines (*L1–L3*) displayed reduced flight ability compared with controls by 1 and 3 wk of age. We compared changes in flight ability within each line between young 2-d-old flies and aged 3-wk-old flies to determine whether functional impairments are progressive, akin to the age-related disease progression observed in DCM patients. All three *S532P* lines exhibited a greater decline in flight ability from 2 d to 3 wk of age compared with controls. Two-way ANOVAs determined that the effects of genotype ($p < 0.0001$) and age ($p < 0.0001$) independently contribute to statistically significant differences among groups, as does the interaction between age and genotype ($p < 0.0001$). Overall, the S532P mutation causes progressive defects in flight ability.

We also assessed heterozygotes to determine whether the S532P mutation causes dominant defects in muscle function, akin to the human condition. Heterozygotes display no defects in flight ability compared with controls at 3 wk of age (Supplemental Table S2), the same age that homozygotes display severe functional defects, indicating that the detrimental effects of the mutation on gross-level IFM function are recessive. Interestingly, β-MyHC alleles that cause dominant DCM in humans typically are not associated with dominant clinical defects in slow skeletal muscles, which express the same MyHC isoform (Villard *et al.*, 2005). Such variances might arise from differences in muscle physiological demands, tissue-specific proteomes, and/or signaling systems.

The S532P mutation induces gene dose–dependent cardiac dilation in *Drosophila*

To determine the effects of the S532P mutation on the fly heart, we crossed the non–His-tagged *Mhc S532P* transgene into the Mhc^1 background. The Mhc^1 allele is null for endogenous myosin in all muscles and must be maintained over a balancer chromosome to prevent death at the embryonic stage (O'Donnell and Bernstein, 1988). While two copies of the *S532P Mhc* transgene rescued lethality of the Mhc^1 homozygotes, the percent eclosion was lower compared with that of wild-type transgenic controls (10.1% for *L1* and 7.5% for *L2* vs. 17.9%, with 33.3% being the predicted percentage of homozygotes). This indicates that expressing the mutant transgene in all muscles in the absence of wild-type *Mhc* reduced survival to the adult stage. Further, the median lifetime of homozygous mutant adults was reduced compared with controls (7 d for *L1* and 4.5 d for *L2* vs. 9 d) (Supplemental Figure S2). Thus, we examined only the hearts of young *S532P* homozygotes. We also examined heterozygotes, which corresponds to the genotype in the human condition.

Young, 4-d-old *S532P/+* heterozygous flies exhibited no differences in diastolic diameters (DD), diastolic intervals (DI), or systolic

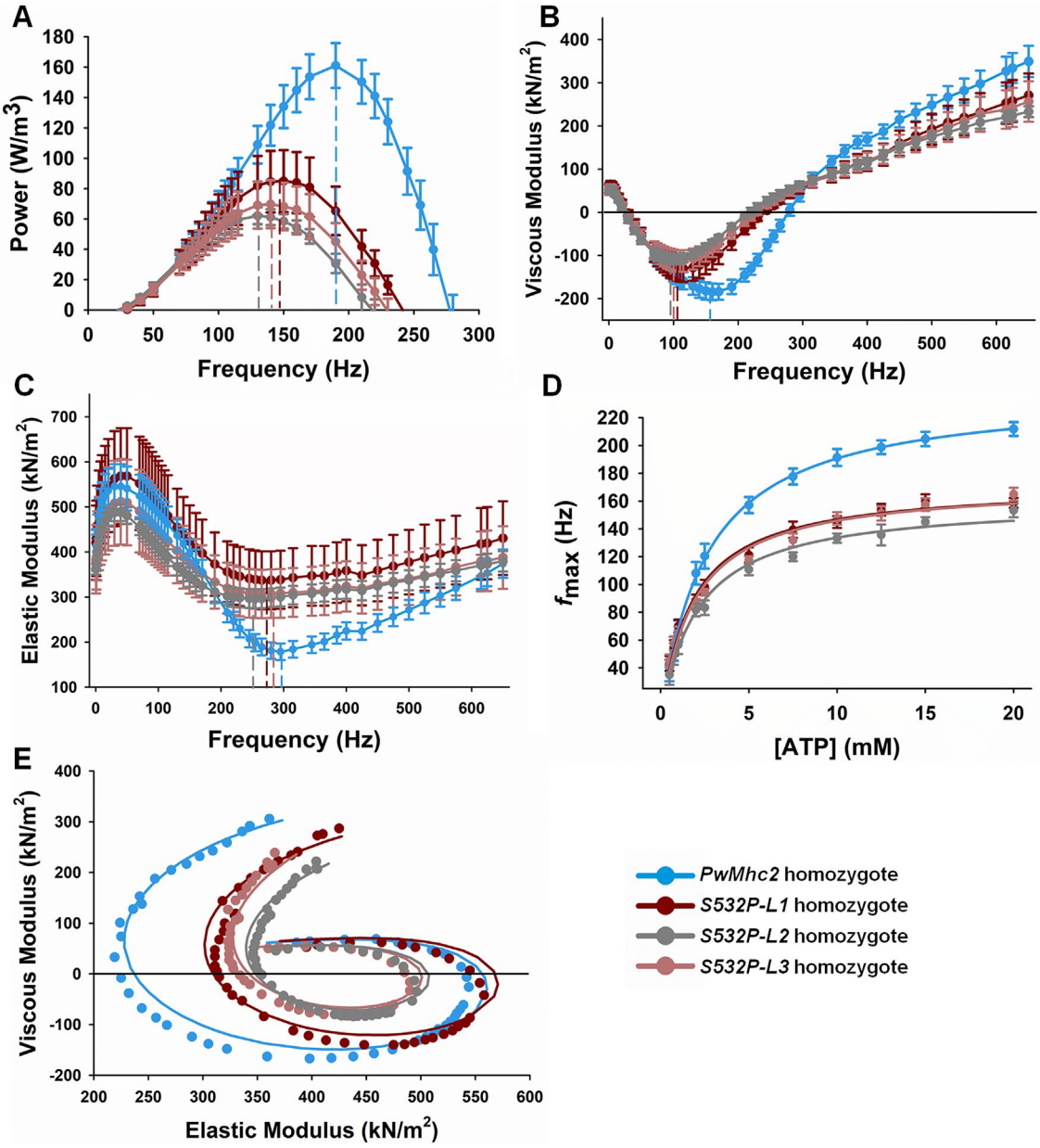

FIGURE 3: Fiber mechanics reveal altered viscoelastic muscle properties and reductions in power output of *S532P* IFMs. (A) Maximum power output and the frequency at which maximum power is generated (f_{max}) were measured by sinusoidal analysis of IFM fibers from homozygotes. f_{max} values are indicated by the vertical dashed lines. (B, C) Changes in viscous modulus (B) and elastic modulus (instantaneous stiffness) (C) were plotted as a function of frequency. Dip frequencies are indicated by vertical dashed lines. (D) Sinusoidal analysis was performed at various ATP concentrations. Values for f_{max} were plotted over changing [ATP] and fitted with a hyperbolic function curve. (E) Viscous moduli vs. elastic moduli were plotted to generate Nyquist plots. The resulting plots were fitted (solid lines) to a three-term equation (Supplemental Figure S1, Eq. 3) to determine exponential rate processes (A, B, and C). Statistical assessments are listed in Table 2. Sample sizes are shown in parentheses: *PwMhc2* homozygote ($N = 10$), *S532P-L1* homozygote ($N = 8$), *S532P-L2* homozygote ($N = 6$), and *S532P-L3* homozygote ($N = 8$). Full genotypes are shown in parentheses: *S532P* homozygote (Mhc^{10}/Mhc^{10}; *P[S532P]/P[S532P]*); *PwMhc2* homozygote (*P[PwMhc2]/P[PwMhc2]*; Mhc^{10}/Mhc^{10}).

intervals (SI) relative to controls (Figure 5, A, E, and F). *S532P-L1/+* flies displayed systolic dysfunction, characterized by increased systolic diameters (SD) (52.41 ± 1.059 vs. 49.29 ± 1.13 μm, $p = 0.046$) and reduced fractional shortening (FS) (0.296 ± 0.010 vs. 0.341 ± 0.009, $p < 0.01$) compared with controls. However, SD and FS did not differ for *S532P-L2/+* (Figure 5, B and C). In contrast, only *S532P-L2/+* exhibited a reduced myogenic heart rate compared with controls (1.83 ± 0.10 beats/s vs. 2.36 ± 0.15 beats/s, $p = 0.0051$) (Figure 5D). We then determined whether expression of two copies of the mutant transgene causes more severe cardiac physiological abnormalities. Both *S532P* homozygous lines exhibited a dilated phenotype, characterized by increases in DD compared with controls (82.805 ± 1.095, $p < 0.0001$ and 75.124 ± 1.675 μm, $p < 0.05$ vs. 70.448 ± 1.965 μm) (Figure 5A). Similar to *S532P-L1/+* flies, *S532P-L1/S532P-L1* flies exhibited systolic dysfunction characterized by increased SD (60.624 ± 1.215 μm vs. 47.764 ± 2.038 μm, $p < 0.0001$)

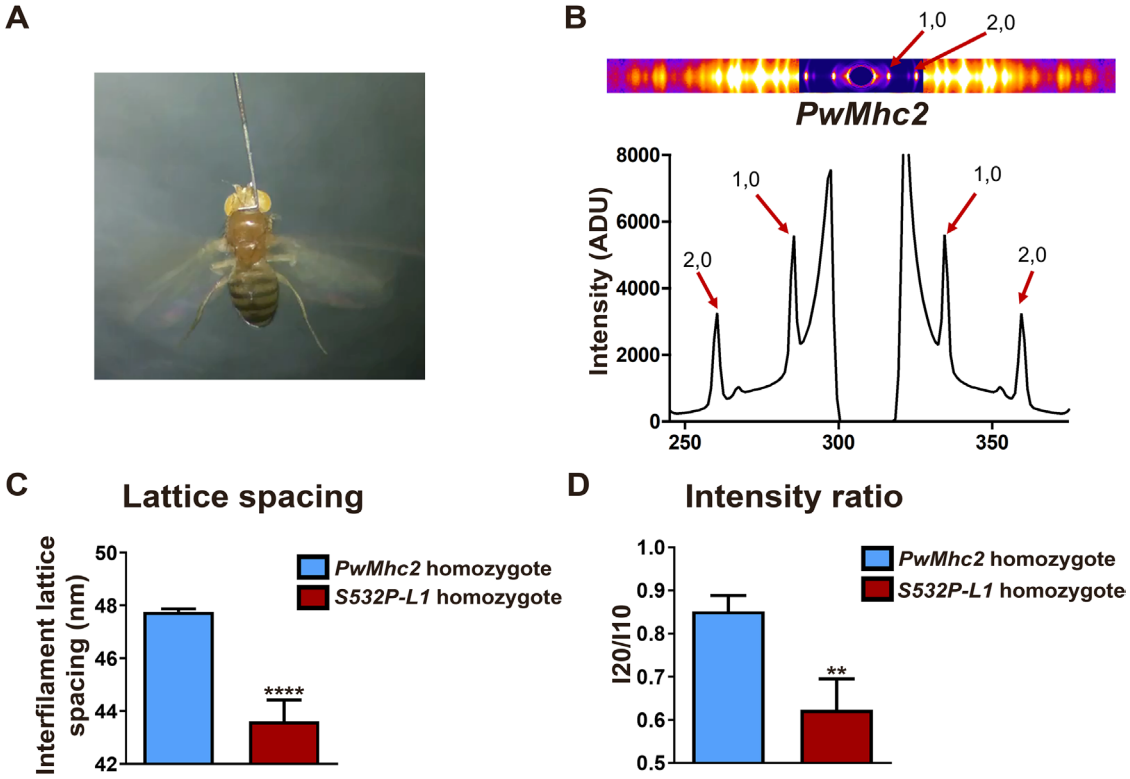

FIGURE 4: Small-angle x-ray diffraction experiments of actively beating IFMs reveal reductions in lattice spacing and in the active number of cross-bridges in *S532P* fibers. The impact of the S532P mutation on lattice spacing and intensity ratio was measured by small-angle x-ray diffraction of thoraces from flies actively beating their wings. (A) Flies were immobilized with an insect pin. (B) Top, equatorial diffraction pattern of a transgenic wild-type fly. Bottom, a one-dimensional intensity trace showing the 1,0 and 2,0 reflection peaks. (C) The interfilament lattice spacing (d_{10}) is reduced in *S532P-L1* IFMs ($N = 7$) compared with *PwMhc2* controls ($N = 15$). (D) The intensity ratios ($I_{2,0}/I_{1,0}$) associated with the number of active cross-bridges are reduced in *S532P-L1* IFMs ($N = 7$) compared with controls ($N = 14$). Data are reported as the mean ± SEM. Statistical significance was determined using Student's *t* tests, where $^{**}p < 0.01$ and $^{****}p < 0.0001$. Full genotypes are shown in parentheses: *S532P-L1* homozygote (Mhc^{10}/Mhc^{10}; *P[S532P]/P[S532P]*); *PwMhc2* homozygote (*P[PwMhc2]/P[PwMhc2]*; Mhc^{10}/Mhc^{10}).

and decreased FS (0.268 ± 0.011 vs. 0.328 ± 0.013, $p < 0.001$) (Figure 5, B and C). Line *L2* did not show differences in these parameters relative to controls. Only *L1* showed an increase in heart rate compared with controls (3.17 ± 0.11 beats/s vs. 2.17 ± 0.14 beats/s, $p < 0.0001$) (Figure 5D). Diastolic and systolic intervals did not differ in either mutant line compared with controls (Figure 5, E and F). Because young homozygotes displayed a dilated phenotype, while age-matched heterozygotes did not, the mutational effects on cardiac dilation were gene dose–dependent in young *S532P* flies. We tested whether aged *S532P/+* flies exhibit cardiac dilation and discovered that 3-wk-old *S532P/+* flies displayed a significantly higher DD compared with controls (74.202 ± 1.327 and 74.796 ± 1.479 vs. 67.209 ± 1.262 µm, $p < 0.001$) (Supplemental Figure S3A). Systolic diameters did not differ for either line compared with controls (Supplemental Figure S3B). Overall, *S532P* flies show cardiac dilation that is influenced by age and genotype, making them a useful model for exploring the cellular pathways associated with DCM pathogenesis.

Finally, we employed transmission electron microscopy to determine whether the S532P mutation affects cardiac ultrastructure. Micrographs of thin sections across the heart tube reveal a layer of cardiac myocytes as well as a layer of supportive ventral longitudinal skeletal muscle cells (Figure 6, A and B). Cardiac myofibrils (MF) are oriented mainly perpendicular to the anterior–posterior axis and contain discontinuous Z-disks (arrows), as standardly observed in this tissue (Melkani *et al.*, 2013; Kaushik *et al.*, 2015; Achal *et al.*, 2016; Bhide *et al.*, 2018; Kronert *et al.*, 2018). The ultrastructural properties of 4-d-old *S532P* homozygous mutant hearts are similar to those of controls, with no obvious signs of myofibrillar disorganization, assembly defects, or degeneration. Dorsal-side and ventral-side cardiac thickness averages do not differ in 4-d-old homozygous mutants compared with controls (Figure 6, C and D). Thus, *S532P/S532P* hearts do not show ultrastructural signs of progressive, pathological DCM remodeling at this age.

DISCUSSION

We introduced the S532P human DCM mutation into the *Drosophila* MHC to determine the feasibility of using this model organism to elucidate biochemical, cell biological, and physiological mechanisms of the disease. The S532P mutation is well-documented to cause DCM in humans. The age of diagnosis (ages 2–57) and severity of symptoms varied in 19 *S532P/+* patients from a single family (Kamisago *et al.*, 2000). Nearly all patients exhibited clinically relevant enlargements in LV end-diastolic and systolic diameters, and some showed deficits in FS. In another report, eight of 15 *S532P/+* patients exhibited enlarged LV end-diastolic diameters and deficits in EF indicative of overt DCM (Lakdawala *et al.*, 2012). In a mouse model of DCM, animals expressing S532P in α-cardiac MyHC (the major ventricular isoform in adult mice) exhibited progressive LV dilation in heterozygotes and early-onset cardiac dilation along with

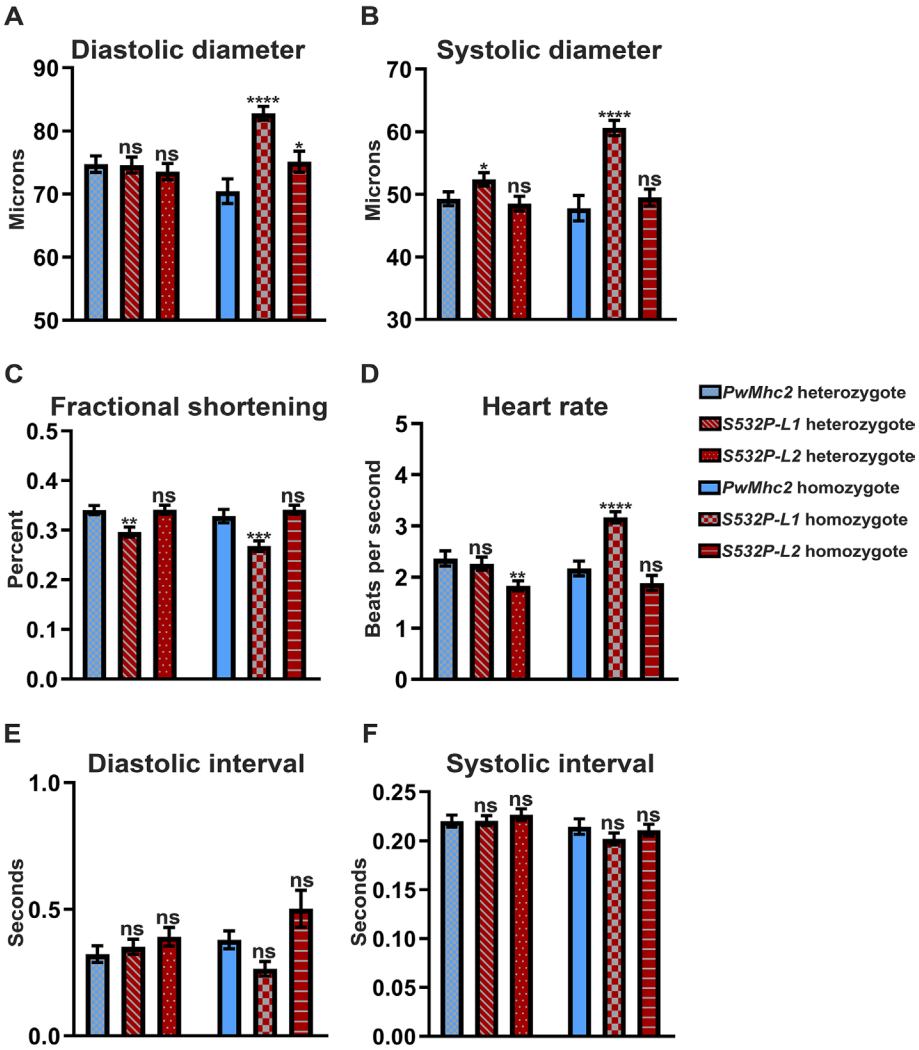

FIGURE 5: *S532P* flies exhibit gene dose–dependent cardiac dilation. (A, B) Cardiac dimensions, (C) fractional shortening, and (D–F) dynamics of 4-d-old *PwMhc2* control or mutant *S532P* heterozygous and homozygous lines (*L1* or *L2*). Values represent mean ± SEM. One-way ANOVAs determined statistical significance compared with controls, where $*p < 0.05$, $**p < 0.01$, $***p < 0.001$, $****p < 0.0001$, and ns = nonsignificant. Sample sizes are listed in parentheses: *PwMhc2* heterozygote ($N = 35$), *S532P-L1* heterozygote ($N = 36$), *S532P-L2* heterozygote ($N = 30$), *PwMhc2* homozygote ($N = 32$), *S532P-L1* homozygote ($N = 33$), *S532P-L2* homozygote ($N = 35$). Full genotypes are shown in parentheses, where "-" indicates that there is no *P* element on the homologous chromosome: *S532P* heterozygote (Mhc^1/+; *P[S532P]/–*); *PwMhc2* heterozygote (*P[PwMhc2]/–*; Mhc^1/+); *S532P* homozygote (Mhc^1/Mhc^1; *P[S532P]/P[S532P]*); *PwMhc2* homozygote (*P[PwMhc2]/P[PwMhc2]*; Mhc^1/Mhc^1).

contractile deficits in homozygotes, suggesting a DCM-causative and gene dose–dependent role of the mutation (Schmitt *et al.*, 2006).

Given that the S532 residue localizes to an α-helix within an actin-binding site (Aksel *et al.*, 2015), we hypothesized that a proline substitution would disrupt actomyosin interactions, possibly by bending or kinking the helix. We observed a trend of lower actin affinity (i.e., higher K_d) in the mutant compared with wild-type myosin using the cosedimentation approach in the absence of nucleotide (Figure 1E). As the effects of the mutation on actin affinity may differ during the chemomechanical cycle, we performed a sinusoidal analysis on skinned IFM fibers to determine rate constants associated with actin binding. The muscle apparent rate constant 2πb was significantly lower in S532P homozygous fibers (Table 2), suggesting that the mutation slows a work-generating step that involves actin attachment and/or the power stroke step. The rate constant 2πc was higher in mutant fibers, suggesting that the mutation enhances the transition out of the A-M-ADP state and/or the following states, causing myosin to detach more quickly from actin. Both of these rate constant changes decrease the amount of time S532P myosin spends bound to actin during the cross-bridge cycle. This lowered duty ratio would reduce the fraction of myosin heads bound to actin and account for the observed decrease in work output (Spudich, 2014). Consistent with this notion, kinetic analyses using recombinant mutant human β-cardiac myosin showed that myosin S532P exhibits a reduction in duty ratio due to a reduced occupancy of the force holding ADP-bound actomyosin state (A-M-ADP) (Ujfalusi *et al.*, 2018). Ujfalusi *et al.* noted that these altered kinetic properties are predicted to reduce contractile function by lowering the load-bearing capacity of the mutant forms, that is, more cross-bridges need to be active to sustain load relative to wild type.

Previous reports that modeled the S532P mutation in mouse α-MyHC support our hypothesis that this mutation interrupts actomyosin interactions. A laser trap assay determined that the step size associated with actin binding was significantly depressed in S532P mouse α-MyHC (Schmitt *et al.*, 2006). Surprisingly, the duration of the time in which myosin remained bound to actin after the power stroke (t_{on}) was longer. However, the authors acknowledged that individual kinetic steps affected by t_{on} could not be determined at the subsaturating levels of ATP used in the assay, because t_{on} is limited by the rates of both MgATP binding and ADP release. Muscle mechanics revealed that the rate constant 2πb is higher in skinned *S532P/+* mouse myocardial fibers (Palmer *et al.*, 2013), contrary to the depressed motor function observed in molecular level studies on myosin isolated from homozygous mutant hearts (Schmitt *et al.*, 2006). Palmer *et al.* (2013) attributed this discrepancy to potential effects of sample preparation, assay design, or differences between genotypes or posttranslational modifications. The rate constant 2πc associated with detachment of myosin from actin was significantly higher in mouse *S532P/+* fibers at intermediate concentrations (0.4–0.8 mM) of Mg-ATP, consistent with our fly model. Minor differences in the actin-binding properties between α-MyHC in mouse *S532P/+* fibers and myosin in *Drosophila S532P/S532P* fibers may be attributed to the effects of genotype or differences between protein backbones. However, our data support a similar overarching conclusion that the S532P mutation reduces power output by affecting actomyosin interactions, particularly time spent strongly bound to actin.

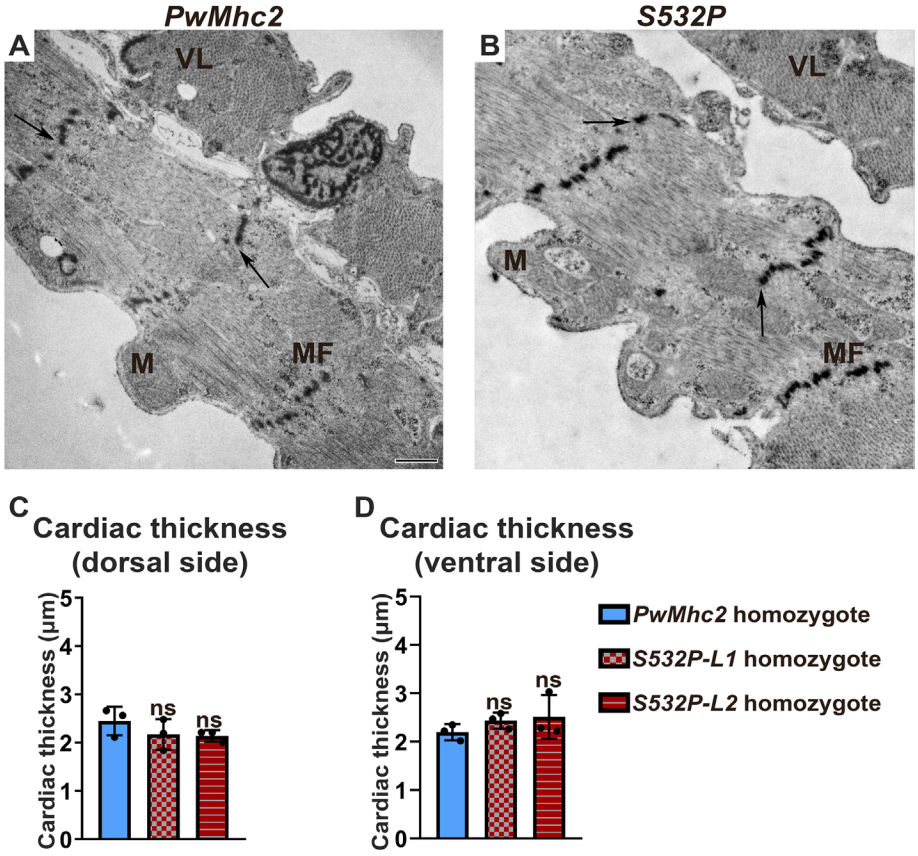

FIGURE 6: The S532P mutation does not affect the organization and stability of cardiac myofibrils. (A, B) Transmission electron micrographs of hearts of 4-d-old *PwMhc2* control or mutant line *S532P-L1* homozygotes in a homozygous *Mhc*^{1}*-null* background. Micrographs show transverse sections of the heart tube between the third and fourth sets of ostia. The arrows indicate discontinuous Z-disks that are characteristic of *Drosophila* cardiac myofibrils. MF: myofibril; M: mitochondrion; VL: supportive ventral longitudinal fibers. Scale bar, 0.5 µm. Cardiac thickness of dorsal-side (C) and ventral-side (D) areas of the heart were measured using ImageJ. Three flies were tested for each line. Values represent mean ± SD. Student's *t* tests determined statistical significance compared with controls, where ns = nonsignificant. Full genotypes are shown in parentheses: *S532P* homozygote (*Mhc*^{1}/*Mhc*^{1}; *P[S532P]/P[S532P]*); *PwMhc2* homozygote (*P[PwMhc2]/P[PwMhc2]*; *Mhc*^{1}/*Mhc*^{1}).

Our observation of S532P myosin's reduced actin-stimulated ATPase activity (V_{max}) in the absence of changes in basal Mg-ATPase activity (Figure 1, B and C, and Supplemental Table S1) is in concordance with the reduced rate of S532P myosin's actin binding and/or an attenuated ability of actin to increase the P_i release rate. On the basis of these data, we postulate that the S532P mutation induces a conformational change that impairs closure of the actin-binding cleft and slows P_i release. This is expected to lower the rate of transition from weak to strong actin binding (Muretta *et al.*, 2013; Houdusse and Sweeney, 2016), consistent with our finding that apparent rate constant 2πb is lower in skinned IFM mutant fibers (Table 2).

Similar to our fly model for S532P myosin, a W546A mutation of chicken gizzard heavy meromyosin located within a helix structurally analogous to the β-MyHC S532–containing helix dramatically lowers the V_{max} of actin-stimulated ATPase activity without altering K_m (Onishi *et al.*, 2006). The authors of this study suggest that the mutation interrupts actin cleft closure, slowing the rate of P_i release without affecting actin affinity. Consistent with this, expression of the S532P mutation in human β-MyHC short subfragment-1 (sS1) (Aksel *et al.*, 2015) and mouse α-MyHC (Schmitt *et al.*, 2006) lowered the V_{max} of actin stimulation, though the difference was not significant for α-MyHC. The K_m of actin stimulation was significantly higher for human β-MyHC sS1 (Aksel *et al.*, 2015), suggesting lower actin-binding affinity, while K_m was unchanged for α-MyHC (Schmitt *et al.*, 2006). These data agree with our observations that one effect of the S532P mutation is to decrease the steady-state ATPase rate.

We hypothesized that expression of S532P myosin in *Drosophila* would yield muscle fiber functional deficits, as previous reports revealed that the S532P mutation reduces the loaded actin sliding velocity (Aksel *et al.*, 2015) and force-generating capacity (Ujfalusi *et al.*, 2018) of human β-MyHC sS1. Additionally, the maximum isometric force of S532P mouse α-MyHC was significantly reduced in a laser trap assay (Debold *et al.*, 2007). Indeed, our muscle mechanical analyses revealed depressed power production in S532P IFM fibers (Figure 3A and Table 2). The lower power was attributed to a reduction in the frequency at which maximum power was produced, suggesting slower overall muscle speed, as well as a reduction in work production (Figure 3B) associated with a decreased amount of time spent in the strongly bound states (Table 2).

Our small-angle x-ray diffraction data from actively contracting IFM suggest that the S532P mutation significantly reduces the $I_{2,0}/I_{1,0}$ equatorial intensity ratio relative to transgenic wild-type controls (Figure 4D). This indicates that the myosin heads are less associated with the thin filament and more associated with the thick filament backbone under contracting conditions, suggesting that, on average, fewer cross-bridges are interacting with actin during steady-wing-beat conditions than in control muscle. Consistent with this, an increase in the rate constant 2πc in IFMs (Table 2) suggests that the mutation enhances the transition out of the A-M-ADP state and/or the following states, causing myosin to detach more quickly from actin. The decrease in lattice spacing in active mutant IFMs (Figure 4C) may further impact the probability of productive actomyosin interactions (Figure 3A and Table 2). Multiple factors are known to reduce cross-bridge binding that could be altered by the S532P mutation. These include dephosphorylation of the myosin regulatory light chain (Irving and Maughan, 2000), the enhanced formation of the super-relaxed state (McNamara *et al.*, 2015) in which the myosin heads interact to prevent actin binding (Zoghbi *et al.*, 2008), and decreased levels of tension that stabilize the off state of the thick filament (Linari *et al.*, 2015). Again, our data are consistent with the notion that the S532P mutation reduces the rate of actin binding and increases the rate of actin detachment, leading to fewer attached heads at a given moment and reduced power output.

Mutant S532P flies exhibited an age-related decline in flight ability (Table 1). These data are consistent with the progressive nature of reduced cardiac function in human DCM patients. However, the

ultrastructural properties of IFMs are normal in 3-wk-old *S532P/S532P* flies (Figure 2), suggesting that the severe reductions in muscle function at this age are not due to structural deterioration of myofibrils. The causes of locomotory decline with age in our fly models remain unknown. Age-related changes in gene expression (Landis *et al.*, 2004; Zahn *et al.*, 2006; Carlson *et al.*, 2015), protein expression (Fleming *et al.*, 1986), as well as damage to lipids, proteins (Das *et al.*, 2001; Miller *et al.*, 2008), and organelles (Miller *et al.*, 2008), may play a role in exacerbating muscle functional deficits. In contrast, heterozygotes display normal flight ability at 3 wk of age (Supplemental Table S2). The maintenance of flight ability in heterozygotes indicates that the mutant myosin is incorporated into the myofibril, because both copies of *Mhc* are required to prevent defective IFM structure and function (O'Donnell and Bernstein, 1988).

Though differences in protein backbone and muscle physiology are expected to influence the effects of the S532P mutation, we expect that our skeletal muscle data are relevant to disease mechanisms in cardiomyocytes because the mutation is located in a well-conserved actin-binding site. Consistent with the observed phenotypes in the two muscles of S532P, a hypoactive A261T myosin mutation that lowers actin affinity, reduces actin-activated ATPase activity, causes defects in flight ability, and yields cardiac dilation in *Drosophila* does not lead to structural deterioration of IFMs (Cammarato *et al.*, 2008; Bloemink *et al.*, 2011).

S532P flies exhibited cardiac dilation that is gene dose–dependent (Figure 5A). Similarly, *S532P/S532P* mice exhibited more severe cardiac dilation compared with *S532P/+* mice (Schmitt *et al.*, 2006). Contractile deficits were reported in isolated mouse α-MyHC S532P cardiomyocytes at an age before cardiac dilation, suggesting an association between cardiac dilation and systolic dysfunction in mice (Schmitt *et al.*, 2006). *S532P-L1/S532P-L1* and *S532P-L1/+* flies exhibited deficits in fractional shortening at 4 d of age (Figure 5C). Thus, it is possible that systolic dysfunction is a contributing factor to cardiac dilation observed in this line. Though the molecular mechanisms of muscle contraction are similar between *Drosophila* and human hearts, phenotypic outcomes may vary between species due to differences in cardiac morphology and physiology (Ocorr *et al.*, 2007; Nishimura *et al.*, 2011; Rotstein and Paululat, 2016). Further transcriptomic or proteomic studies are needed to explore cellular pathways causative of cardiac dilation in S532P hearts.

Cardiac ultrastructure is normal in 4-d-old *S532P/S532P* flies (Figure 6, A and B), suggesting that cardiac physiological abnormalities induced by the hypoactive S532P DCM myosin form are not caused by defects in myofibrillar assembly or maintenance. This is consistent with our data that relaxed IFM ultrastructure is normal in *S532P/S532P* flies (Figure 2). Cardiomyocyte disarray was also absent in a *S532P/+* patient (Kamisago *et al.*, 2000) and in α-MyHC S532P mice (Schmitt *et al.*, 2006). Cardiac thickness did not differ in young *S532P/S532P* flies compared with controls (Figure 6, C and D), suggesting that cardiac dilation observed at this age is not associated with a loss of cardiac myofibrils that is characteristic of pathogenic DCM. However, the increased diastolic diameters denote an increase in the length of the opposing cells that comprise the wall of the heart tube, indicating eccentric cardiomyocyte remodeling. In sum, our studies suggest that functional defects in the DCM muscle arise from aberrant contractile protein interactions that may be exacerbated over time and lead to heart failure in humans.

Many small molecules have been developed and tested to specifically offset the effects of myosin mutations that enhance or diminish the motor's chemomechanical properties, as recently reviewed (Alsulami and Marston, 2020). Therefore, assuming conserved binding of these ligands to either *Drosophila* skeletal or cardiac myosin, fly muscle could be exploited to inexpensively and rapidly test for beneficial effects of compounds before follow-up verification in more complex and less efficient vertebrate models.

Overall, we produced the first *Drosophila* model of myosin-induced DCM and gained insights into the mechanistic basis of disease. The ability to pursue an integrative analysis from the level of the isolated mutant protein through muscle mechanical, ultrastructural, and physiological assays verified mammalian studies regarding ATPase activity and myofibril ultrastructure and yielded novel insights regarding cross-bridge kinetics. Our fly model thus provides a platform for readily validating putative human DCM myosins as leading to phenotypes consistent with DCM and for employing a genetic background that obviates modifier gene effects often observed in human DCM families. Combining our current results with our previous studies on hypertrophic and restrictive cardiomyopathy mutations (Achal *et al.*, 2016; Kronert *et al.*, 2018), we have demonstrated that *Drosophila* is useful for classifying myosin cardiomyopathy mutations into those that either enhance or depress motor function.

MATERIALS AND METHODS

Request a protocol through *Bio-protocol*.

Generation and validation of mutant genomic DNA fly lines

For transgene construction, the PwMhc2 wild-type genomic Mhc construct (Swank *et al.*, 2000) was digested with *Eag*I to yield pMhc 5′ and pMhc 3′ fragments, which were subsequently gel isolated and ligated into *Eag*I sites in the pCasper vector (Thummel and Pirrotta, 1992) to produce pMhc 5′ and pMhc 3′ subclones. The pMhc 5′ subclone was digested with *Pst*I and *Eag*I to produce a pPstEag subclone containing a 2.4-kb insert, which was gel isolated and ligated into a *Pst*I and *Eag*I site in the pBluescriptKS (Stratagene, La Jolla, CA) vector. The pPstEag subclone was further digested with *Nco*I and *Sac*I. A 0.8-kb *Nco*I-*Sac*I fragment containing *Mhc* exon 10 was gel isolated and ligated into a *Nco*I-*Sac*I site in the pLitmus vector to produce a pNcoSac subclone. Oligonucleotide-directed mutagenesis was performed using the QuikChange kit (Stratagene, La Jolla, CA) on the pNcoSac subclone to change the codon in *Drosophila Mhc* that corresponds to the *MYH7 S532P* nucleotide transition. The following forward (+) and reverse (–) primers were used for mutagenesis, with the mutated codon underlined:

S532P (+): 5′-CCCATGGGTATCTTGCCCATCCTGGAGGAAG-3′

S532P (-): 5′-CTTCCTCCAGGATGGGCAAGATACCCATGGG-3′

The mutated exon of the pNcoSac resulting S532P subclone was sequenced for confirmation and was digested with *Nco*I and *Sac*I. The 0.8-kb mutant insert was used to replace the wild-type *Nco*I-*Sac*I fragment of pPstEag. The resulting clone was digested with *Eag*I and *Sph*I, and the 2.0-kb insert was gel isolated and ligated into an *Eag*I-*Sph*I site of pMhc 5′. For the final cloning step, the 19.2-kb 5′ *Mhc* fragment carrying the S532P mutation was removed from its vector by *Eag*I digestion and ligated to a 3′ *Mhc* fragment in a pCaSpeR *P* element vector containing the *miniwhite* (w^+) selectable eye color marker. The final plasmid was purified using the QIAfilter Plasmid Maxi Kit (Qiagen, Hilden, Germany), and the entire *Mhc*-coding region was sequenced for verification by Eton Bioscience (San Diego, CA).

Embryonic injection was performed by BestGene (Chino Hills, CA) to incorporate the transgenic insert randomly into the germline via *P* element transformation (Bischof *et al.*, 2007). A total of 39 transgenic lines were obtained. Several lines mapping to the third

chromosome were crossed into the *Mhc*^{10} myosin-null background that is null for endogenous myosin in IFMs and jump muscles (Collier *et al.*, 1990). Lines that mapped to the second chromosome were not used because it contains the endogenous *Mhc* gene.

PAGE– was performed to determine MHC protein levels in these lines, by comparing the ratio of myosin to actin between transgenic flies and *yw* (wild type) controls, as described previously (Suggs *et al.*, 2007). Each lysate consisted of six upper thoraces of 0–2-d-old flies. Only lines with wild-type MHC protein levels were chosen for further experiments.

RT-PCR (reverse transcription polymerase chain reaction) confirmed the expression of RNA encoding the mutant protein and the absence of endogenous myosin expression in IFMs. RNA was isolated from 2-d-old upper thoraces using the RNeasy kit by Qiagen (Hilden, Germany). The Protoscript cDNA synthesis kit was employed to generate cDNAs, using 500 ng of RNA and 100 ng of the specific reverse (–) primer shown below. cDNA was amplified using *Mhc*-specific primers to confirm the absence of alternative splicing defects in these lines:

Exons 2–8:

(+) 5′-TGGATCCCCGACGAGAAGGA-3′

(-) 5′-GTTCGTCACCCAGGGCCGTA-3′

Exons 8–10:

(+) 5′-CGATACCGCCGAGCTGTACAG-3′

(-) 5′-CAGCTGGTGCATGACCAAGTGGGC-3′

Exons 8–12:

(+) 5′-TCTGGATACCCAGCAGAAGCGT-3′

(-) 5′-GAGCTTCTTGAAGCCCTTACGG-3′

Exon 15:

(+) 5′-CTCAAGCTCACCCAGGAGGCT-3′

(-) 5′-GGGTGACAGACGCTGCTTGGT-3′

PCR was performed using 3 µl of cDNA and 200 ng of each forward and reverse primer, under the following conditions: 120 s at 98°C and then 30 cycles of 20 s at 98°C, 30 s at 55°C, and 2 min at 68°C. RT-PCR products were sequenced by Eton Bioscience (San Diego, CA). For simplicity, lines *S532P-9*, *S532P-23*, and *S532P-34* were respectively renamed as *S532P-L1*, *S532P-L2*. and *S532P-L3*.

Myosin purification and ATPase assay

Myosin purification. Full-length myosin was purified from IFMs as described previously (Swank *et al.*, 2001) with minor modifications. Dorsal longitudinal IFMs were dissected from 80–120 transgenic flies in 1 ml York Modified Glycerol (YMG: 20 mM potassium phosphate buffer, pH 7.0, 1 mM EGTA (ethylene glycol-bis(β-aminoethyl ether)-*N*,*N*,*N*′,*N*′-tetraacetic acid), 2 mM $MgCl_2$, 50% glycerol, 20 mM dithiothreitol [DTT], and Roche complete mini protease inhibitor [1 tablet per 10 ml solution]) on ice. The sample was centrifuged at 15,000 × *g*, 5 min, 4°C, and the pellet was resuspended in YMG containing 2% Triton-X. The sample was incubated for 30 min on ice to permeabilize cell membranes and then centrifuged at 15,000 × *g*, 5 min, 4°C. Triton-X was removed by resuspending the pellet in 1 ml YM buffer (same as YMG but without glycerol). The sample was centrifuged at 15,000 × *g*, 5 min, 4°C. The pellet was resuspended in 82.5 µl of myosin extraction buffer (1.0 M KCl, 50 mM potassium phosphate buffer, pH 6.8, 10 mM sodium pyrophosphate, 5 mM $MgCl_2$, 0.5 mM EGTA, and 20 mM DTT) for 15 min and centrifuged at 15,000 × *g*, 5 min, 4°C. The supernatant was removed, and the pellet was discarded. Extracted myosin in the soluble portion was precipitated by diluting the KCl concentration to 40 mM with deionized water and incubating for 16 h at 4°C. The sample was centrifuged (Beckman TLA-100.3; 100,000 × *g*, 20 min, 4°C), and the pellet was dissolved in 13.5 µl buffer (2.4 M KCl, 100 mM histidine, 0.5 mM EGTA, 20 mM DTT, pH 6.8). KCl was slowly diluted to 300 mM to precipitate actomyosin, and the sample was centrifuged (Beckman TLA-100.3; 60,000 × *g*, 25 min, 4°C). The supernatant was separated, and KCl was diluted to 30 mM to precipitate myosin. Following centrifugation (Beckman TLA-100.3; 100,000 × *g*, 25 min, 4°C), the pellet was resuspended in 33 µl myosin storage buffer (0.5 M KCl, 20 mM MOPS, pH 7.0, 2 mM $MgCl_2$, and 20 mM DTT), and the purified myosin was diluted to a concentration of 2 mg/ml.

ATPase assay. The ATPase activity of full-length myosin was measured using [γ-^{32}P]-ATP as described previously (Swank *et al.*, 2001). For Ca-ATPase activity, a total of 2 µg of myosin was incubated in 10 mM imidazole, pH 6.0, 100 mM KCl, 10 mM $CaCl_2$, and 1 mM [γ-^{32}P]-ATP at room temperature for 15 min. To determine Mg^{2+} basal and actin-stimulated Mg-ATPase activities, 2 µg of myosin was incubated in 10 mM imidazole, pH 6.0, 20 mM KCl, 0.1 mM $CaCl_2$, 1 mM $MgCl_2$, and 1 mM [γ-^{32}P]-ATP in the absence or presence of increasing concentrations of chicken F-actin (0.1–2 µM) at room temperature for 25 min. Following centrifugation, the organic phase containing [γ-^{32}P]-ATP was extracted by adding aliquots of the soluble portion to 0.5 ml of 5% ammonium molybdate, 2 ml of 1.25 N $HClO_4$, and 2.5 ml of isobutanol–benzene (1:1). A total of 1 ml of the organic phase containing [γ-^{32}P]-ATP was assayed for radioactivity with a scintillation counter. Mg^{2+} basal ATPase activities were subtracted from actin-activated ATPase values, which were fitted with the Michaelis–Menten equation to determine actin-stimulated ATPase activity (V_{max}) and actin affinity relative to ATPase (K_m).

Generation of a mutant His-tagged myosin line

We produced a fly line expressing a His-tagged mutant version of the indirect flight muscle myosin isoform (IFI) to obtain S532P myosin S1 in quantities sufficient for cosedimentation experiments. To this end, we utilized a pAttB 6HisIFI plasmid that contains the *Actin-88F* promoter, an amino-terminal His tag, a tobacco etch virus (TEV) protease recognition site (for removal of the His tag), and cDNA encoding the IFI motor domain, as well as genomic DNA-encoding MHC exons 12–19 along with their affiliated introns and polyadenylation sites (Caldwell *et al.*, 2012). The pAttB 6HisIFI plasmid was digested using *Xba*I and *Sbf*I to produce a pXbaSbf subclone containing a 6.3-kb fragment. The *Xba*I-*Sbf*I fragment was ligated into a *Xba*I-*Sbf*I site in the pLitmus vector. The pXbaSbf subclone was digested with *Nco*I and *Hin*dIII to produce a 2.6-kb fragment containing *Mhc* exon 10. The fragment was ligated into a *Nco*I-*Hin*dIII site in the pLitmus vector. Oligonucleotide-directed mutagenesis was performed using the QuikChange kit (Stratagene, La Jolla, CA) on the resulting subclone to change the codon in *Drosophila Mhc* that corresponds to the *MYH7 S532P* nucleotide transition. The following forward (+) and reverse (–) primers were used, with the mutated codon underlined:

S532P (+): 5′-CACCATGGGTATCTTGCCCATCCTGGAGGAAGA-3′

S532P (–): 5′-TCTTCCTCCAGGATGGGCAAGATACCCATGGTG-3′

The mutated exon in the resulting isolated plasmid was sequenced for confirmation. The plasmid was digested with *Nco*I and *Hin*dIII, and the 2.6-kb fragment was used to replace the wild-type *Nco*I-*Hin*dIII fragment of the pXbaSbf cloning intermediate. The entire construct was digested with *Xba*I and *Sbf*I, and the 6.3-kb

mutant fragment was used to replace the wild-type *Xba-Sbf* fragment of the pAttB 6HisIFI clone to produce the final pAttB 6HisIFI S532P clone. The pAttB vector contains a *miniwhite* (w^+) selectable eye color marker that restores eye color in a white-eyed genetic background, as well as PhiC31 integrase AttB recognition sites. The final cloned DNA was purified using the QIAfilter Plasmid Maxi Kit (Qiagen, Hilden, Germany) and sequenced for verification by Eton Bioscience (San Diego, CA). Targeted chromosomal site insertion was performed by BestGene (Chino Hills, CA) using the PhiC31-mediated transgenesis system (Bischof *et al.*, 2007). One transgenic line containing a third chromosome-targeted insert was produced.

Transgenic flies were crossed into a Mhc^{10} background that is null for endogenous myosin in IFMs (Collier *et al.*, 1990). Myosin protein levels are expressed at ~78% relative to wild-type *yw* flies in upper thoraces, as determined by SDS–PAGE and densitometry analysis (Suggs *et al.*, 2007). RT-PCR was employed to verify that the *Mhc* transcripts produced by this line contain the appropriate nucleotide transition. RNA isolation, cDNA synthesis, and PCR amplification were performed as described above for the non–His-tagged lines, using the following primer pair:

(+) 5′-TCTGGATACCCAGCAGAAGCGT-3′

(–) 5′-CAGCTGGTGCATGACCAAGTGGGC-3′

RT-PCR products were sequenced by Eton Bioscience (San Diego, CA).

Bulk S1 purification from His-tagged flies

His-tagged myosin was isolated from IFMs of homogenized flies using a series of salt-based extractions and Ni-column chromatography (Caldwell *et al.*, 2012). Myosin was extracted from adults (<1 d old) that were collected daily, flash frozen using liquid nitrogen, and stored at –80°C. A total of 36 g of flies was divided between two tubes and homogenized (OMNI International Homogenizer and 10 mm stainless steel probe) in a low-salt homogenization buffer (HB; 0.5% Triton X-100, Roche complete protease inhibitor cocktail tablets [1 tablet/50 ml solution], 12.5% sucrose, 40 mM NaCl, 10 mM imidazole-Cl, 2 mM $MgCl_2$, 0.2 mM EGTA, and 1 mM DTT, at pH 7.2). Before solubilization of myosin, a series of centrifugation steps (Beckman Ti-45 rotor; 40,000 rpm, 1.5 h each, 4°C) were performed to clarify the soluble portion of the homogenate. The supernatants were discarded following each centrifugation. After the first two centrifugations, the pellets containing the insoluble myosin were homogenized in HB. After the third centrifugation step, the pellets were homogenized in high-salt myosin extraction buffer (MEB; 500 mM NaCl, 20 mM sodium phosphate buffer, 20 mM imidazole-Cl, pH 7.2), sonicated with 50 brief pulses at setting 5, 50% duty cycle (Fisher Scientific Sonic Dismembrator Model 100, micro tip), and incubated for 30 min on ice. Following centrifugation (Beckman Ti-45 rotor; 40,000 rpm, 40 min, 4°C), the pellets containing the exoskeleton and cellular debris were discarded. The soluble portions were diluted with 4 mM DTT to a NaCl concentration of 75 mM, incubated for 4 h on ice to precipitate myosin, and centrifuged as before. The pellets were resuspended in 60 ml MEB (OMNI International Homogenizer with plastic tip), and the extracted myosin was filtered and further diluted with 390 ml MEB.

His-tagged myosin was purified using Ni-affinity chromatography (HisTrap HP 5 ml column and ÄKTA pure system by GE Life Sciences). Following sample binding, the Ni column was washed with 30 ml MEB and the sample was eluted in 30 ml elution buffer (500 mM NaCl, 20 mM sodium phosphate buffer, 250 mM imidazole-Cl, pH 7.4). His-tagged myosin was collected in 2 × 2 ml peak fractions, and myosin was precipitated by dilution with a no-salt solution containing 4 mM DTT to 94 mM NaCl.

For purification of the myosin motor domain (subfragment 1: S1), precipitated myosin was centrifuged (Beckman TLA-100.3 rotor; 68,000 rpm, 50 min, 4°C) and pellets were resuspended in digestion buffer (120 mM NaCl, 20 mM NaPi, 1 mM EDTA, 4 mM DTT, pH 7.0). The S1 fragment was clipped using α-chymotrypsin (Worthington Biochemical Corp.; 0.18 mg/ml per 67.8 activity units, 6 min, 20°C), which was previously shown to also remove the His tag at the TEV cut site (Caldwell *et al.*, 2012). To quench the reaction, phenylmethylsulfonyl fluoride was added to a final concentration of 1.5 mM. Samples were centrifuged (Beckman TLA-100.3 rotor; 68,000 rpm, 50 min, 4°C) to remove insoluble rod fragments and uncut myosin from the soluble S1 fraction. To further purify S1, size exclusion chromatography was performed using the ÄKTA Pure system with a 16/600 column packed with Superdex 200. A centrifugal filter (Amicon Ultra-4 ml 10,000 MWCO) was used to concentrate peak S1 fractions to 2–6 mg/ml.

Actin cosedimentation

The binding affinity of S1 to F-actin was determined by actin cosedimentation as described previously (Dose *et al.*, 2007; Taft *et al.*, 2013), with slight modifications. F-actin was polymerized from frozen chicken G-actin stocks and stabilized with a 1:1 M ratio of phalloidin. S1 was purified using the bulk His-tagged myosin purification procedure described above. Subsequently, S1 was centrifuged (Beckman TLA-100.3 rotor; 70,000 rpm, 60 min, 4°C) to remove insoluble aggregates. The protein concentration in the soluble portion was determined by spectrophotometry, and it was diluted to 25 μM. S1 (1.5 μM) was incubated with increasing concentrations of phalloidin-stabilized F-actin (0, 0.4, 0.6. 0.8, 1, 1.2, 1.4, 1.6, 1.8, 2, 3, and 4 μM) in cosedimentation buffer (100 mM NaCl, 200 mM sodium phosphate, 5 mM $MgCl_2$, 4 mM DTT, pH 7.0) in a total volume of 25 μl. The cosedimentation buffer contained an intermediate salt concentration (100 mM NaCl) to promote the solubility of myosin S1. Samples were incubated for 15 min on ice and centrifuged (Beckman TLA-100.3 rotor; 70,000 rpm, 60 min, 4°C). Soluble fractions were separated from pellet fractions, and pellets were resuspended in 25 μl of the cosedimentation buffer. Samples were applied to a 10% SDS–polyacrylamide gel. Gels were stained with the GelCode Blue Stain Reagent, destained, scanned on an Epson Perfection 1640SU scanner using VueScan software (Hamrick), and analyzed using the Un-Scan-It (Silk Scientific) software package as reported previously (Price *et al.*, 2002). To calculate the bound fraction in actomyosin pellet samples, the density of S1 in the pellet fraction relative to total protein content was determined, and the fraction of pelleted S1 in S1-only controls was subtracted from this value. Bound fractions were plotted over increasing F-actin concentrations and fitted to a hyperbolic function, where K_d was defined as the F-actin concentration required to reach half maximal binding (B_{max}).

Small-angle x-ray diffraction

X-ray diffraction experiments on IFMs were carried out at the BioCAT beamline 18ID at the Advanced Photon Source, Argonne National Laboratory (Fischetti *et al.*, 2004). The x-ray beam energy was set to 12 keV (0.1033 nm wavelength) at an incident flux of ~10^{13} photons/s. The beam was focused to ~150 × 30 μm at the detector. The distance between the sample and the detector was set at 3 m. One-day-old non–His-tagged flies were anesthetized by CO_2 and glued to an insect pin, which allowed movement of the wings and legs (Figure 4A). The restoration of jumping and walking abilities was confirmed following a short recovery period. Each fly was

mounted so that its thorax was aligned perpendicular to the x-ray beam. The experimental setup was described in further detail by Irving and Maughan (2000). The x-ray diffraction patterns from DLMs were obtained while the wings were beating during tethered flight at room temperature. Because the myofilament lattice spacing in *Drosophila* IFM was previously reported to remain constant over the wing-beat cycle (Irving and Maughan, 2000), it is not necessary to isolate a particular phase of the wing-beat cycle to establish the lattice spacing under contracting conditions in our experiments.

The equatorial reflections in the two-dimensional x-ray patterns were converted to one-dimensional intensity projections along the equator. The ratio of 1,0 and 2,0 intensities ($I_{2,0}/I_{1,0}$) was measured to estimate shifts of molecular mass from the thick filament to the thin filament; an increase in $I_{2,0}/I_{1,0}$ ratio indicates mass shift of the cross-bridges. The peak intensity, widths, and peak separations for the 1,0 and 2,0 equatorial reflections were estimated using a nonlinear least-squares fitting procedure. The separation of the 1,0 equatorial reflections was transformed into the distance between the lattice planes of the thick filaments ($d_{1,0}$) providing the center-to-center distance between thick filaments (Miller *et al.*, 2008). Axial spacing was calibrated using the diffraction ring from silver behenate at 5.8380 nm.

Muscle mechanics

Detailed procedures for mechanics experiments were as described previously (Swank, 2012).

IFM fiber preparation. Dorsal longitudinal IFM fibers were dissected from 3d-old females in skinning solution (pCa 8.0, 5 mM MgATP, 1 mM free Mg^{2+}, 0.25 mM phosphate, 5 mM EGTA, 20 mM *N,N*-bis(2-hydroxyethyl)-2-aminoethanesulfonic acid [BES, pH 7.0], 175 mM ionic strength [adjusted with sodium methanesulfonate], 1 mM DTT, 50% glycerol, and 0.5% Triton X-100). Fiber bundles were demembranated for 1 h at 6°C and then transferred to storage solution (same as skinning solution but without Triton X-100). Individual fibers were separated from the IFM bundle and split in half longitudinally with tungsten wire probes. Both ends of the fiber were fastened with aluminum foil t-clips. The fiber was transferred to a mechanics rig, submerged in relaxing solution (pCa 8.0, 12 mM MgATP, 30 mM creatine phosphate, 600 U/ml creatine phosphokinase, 1 mM free Mg^{2+}, 5 mM EGTA, 20 mM BES at pH 7.0, 1 mM DTT; 200 mM ionic strength [adjusted with sodium methanesulfonate]), and then hooked onto a force transducer and servo motor.

All measurements were obtained at 15°C. The fiber was stretched until the slack was removed. The fiber length between the t-clips was measured, and the fiber was stretched by 5% of its initial length. The width and height of the fiber were subsequently measured, and the cross-sectional area was calculated assuming an ellipsoid shape. The fiber was activated by partially exchanging the bathing solution with activating solution (same as relaxing solution, with pCa adjusted to 4.0) to bring the pCa to 5.0. The fiber was stretched in 2% increments (relative to the fiber length between the t-clips) until maximum power was obtained (Supplemental Figure S1, Eq. 2), in order to determine the optimal fiber length for performing the mechanical experiments.

Sinusoidal analysis and muscle apparent rate constants. The muscle was oscillated with a small-amplitude sine wave (0.125% muscle length, peak to peak) at frequencies ranging from 0.5 to 650 Hz. For each frequency, the amplitude and phase differences associated with the sinusoidal tension response and length change were calculated to determine the complex modulus (Kawai and Brandt, 1980; Dickinson *et al.*, 1997; Swank, 2012). The complex modulus can be further separated into the viscous and elastic moduli. The viscous modulus is the out-of-phase component in the Nyquist plot (Figure 3E) and from which work and power produced by the fiber can be calculated (Supplemental Figure S1, Eqs. 1–2). The elastic modulus represents an in-phase component of the complex modulus and is influenced by the spring-like properties of the molecular machinery. The complex modulus was fitted to a three-term equation (Supplemental Figure S1, Eq. 3) to determine exponential rate processes (A, B, and C). This equation was obtained from Kawai and Brant (1980) and has been modified to better fit the IFM system (Dickinson *et al.*, 1997). Process A is influenced by the viscoelastic properties of the fiber structure and is not dependent on enzymatic steps of the cross-bridge cycle (Mulieri *et al.*, 2002). Process B reflects work-producing steps related to actin binding. Process C reflects work-absorbing steps before and during detachment from actin. In the Nyquist plot (Figure 3E), processes B and C appear as lower and upper hemispheres, respectively, with associated frequencies b and c. Frequencies b and c were multiplied by 2π to convert from frequency to time (s^{-1}), to determine rate constants associated with work-producing ($2\pi b$) and work-absorbing ($2\pi c$) steps of the cross-bridge cycle.

ATP response experiments. To elucidate cross-bridge kinetics related to ATP-induced dissociation of myosin from actin, the concentration of ATP in the fiber bathing solution was varied from 20 to 0.5 mM while sinusoidal analysis was performed. Values for f_{max} were plotted over changing ATP concentrations and fitted with a hyperbolic function curve to determine V_{max} and a relative measure of ATP affinity (K_m).

Flight tests

Transgenic mutant and control females were reared at 25°C, acclimated to room temperature for 1 h, and flight tested at room temperature. A Plexiglas box (43 cm × 27.5 cm × 43 cm) with a light source at the top was used as a test chamber (Drummond *et al.*, 1991). At least 100 flies from each genetic line/age were tested. Each fly was scored for its ability to fly in an upward (U = 6), horizontal (H = 4), or downward (D = 2) manner toward a light source, and flies with no flight ability received a score of zero ($N = 0$). To calculate the flight index, an equation representative of average flight ability was used: Flight Index (FI) = 6*U/T+4*H/T+2*D/T+0*N/T, where U, H, D, and N represent each fly trajectory listed above and T = total number of flies.

Eclosion and survival analysis

Drosophila were reared on standard fly food at room temperature (22–23°C). Parents were removed after progeny reached the first larval stage. The percentages of females of each genotype that eclosed were recorded daily for 7 d after eclosion of the first adult. Flies were transferred into fresh vials every 3 d for survival analysis. To determine median survival time, the percentage of live females was quantified daily for each genotype and fitted to a Kaplan–Meier curve.

Cardiac physiological analysis

Beating, intact hearts from female flies were surgically exposed in oxygenated artificial hemolymph and recorded for 30 s using a high-speed, high-resolution video camera (Hamatsu Orca Flash 2.8 CMOS or AOS Promon U750) on a light microscope with a 10× immersion lens. Functional parameters were determined using Matlab-based semiautomatic heartbeat analysis software (Ocorr *et al.*, 2007, 2014). For each video, heart chamber dimensions were marked during peak diastole (relaxation) and peak systole (contraction). This was used to determine diastolic (DD) and systolic (SD) diameters. Diastolic and systolic diameters were also utilized to

calculate fractional shortening (FS), to determine heart contractility, using the following equation: FS = (DD – SD)/(DD). M-mode diagrams were obtained to reflect contractile parameters from single pixel tracings of heart wall movements. Parameters related to contractile dynamics included durations for diastolic interval, systolic interval, and heart rate (beats per second). At least 30 hearts per genetic configuration were examined for these parameters, and the mean values for each parameter were statistically compared with those for controls using a one-way or two-way ANOVA.

Transmission electron microscopy of IFMs and hearts

For IFM samples, hemithoraces were dissected and treated with a relaxing solution containing 10 mM EGTA before fixation. For heart samples, the entire dorsal vessel was dissected. Normal, rhythmic beating was verified to avoid analysis of structurally perturbed hearts. Hearts were bathed with a relaxing solution containing 10 mM EGTA and prepared for transmission electron microscopy. The following steps were performed on ice: After incubation in 2 ml primary fixative (3% formaldehyde, 3% glutaraldehyde in 0.1 M sodium cacodylate, pH 7.4), samples were washed 6× in 2 ml wash buffer (0.1 M sodium cacodylate, pH 7.4). Samples were incubated in 2 ml secondary fixative (1% OsO_4, 0.1 M sodium cacodylate buffer, and 10 mM $MgCl_2$, pH 7.4) for 2 h and then washed 3× in HPLC-H_2O. All subsequent steps were performed at room temperature. An acetone dehydration series was carried out at 30 min each: 25%, 50%, 75%, 95%, and 3 × 100% anhydrous acetone. Samples were infiltrated in fresh Epon mix (16.2 ml EM bed-812, 10.0 ml dodecenyl succinic anhydride, 8.9 ml nadic methyl anhydride, 0.6 ml 2,4,6-Tris(dimethylaminomethyl)phenol [DMP-30]) for 2 h each using increasing ratios of Epon:dry acetone (1:3, 1:1, 3:1). Following infiltration in 100% Epon for 16 h, samples were oriented in Epon-filled BEEM capsules and polymerized at 60°C for 1 d under vacuum. Thin sections (50 nm) were cut using a Diatome diamond knife on a Leica Ultramicrotome and collected on Formvar-coated grids. Grids were stained with 2% uranyl acetate for 20 min. Images were obtained at 120 kV on a FEI Tecnai 12 transmission electron microscope.

Quantitative assessments of micrographs

Sarcomere lengths of IFMs were evaluated by measuring the distances between Z-disks using ImageJ (Imagej.nih.gov). A total of 50 sarcomeres per biological replicate ($n = 3$) were analyzed. Measurements of average distances between adjacent thick filaments of IFMs were performed with a custom-written Python script (available upon request). A representative image of the original micrograph (220,000× magnification) is shown in Supplemental Figure S4A. For this procedure, the image was inverted using the cv2.threshold function, and grain noise was minimized using the cv2.adaptivethreshold, cv2.morphologyEx, and cv2.blur functions. Thick filament centers were detected using the cv2.HoughCircles function and the following parameters: HOUGH_GRADIENT, 1, 100, param1 = 100, param2 = 18, minRadius = 9, maxRadius = 15. Detections were overlaid onto the original micrograph to confirm that detections align with thick filament centers (Supplemental Figure S4B). The positions of thick filament centers that were missing from detections were manually added, and erroneous detections were removed. The pixel coordinates of the six closest lattice neighbors from each thick filament center were determined automatically using the Nearest Neighbor Search algorithm. The maximum pixel distance between neighbor detections was set to a value that excludes nonneighbors; a topographical map of neighbor assignments was generated for confirmation (Supplemental Figure S4C). Average neighbor pixel distances were determined for thick filament centers containing six true lattice neighbors, which excluded measurements for thick filament centers located on the edges of micrographs. For each biological sample, average pixel distances between adjacent thick filaments were determined for ≥700 thick filament centers. Values were converted to nanometers using the scale bar, and thick filament distances were averaged for each biological replicate.

Transverse thin sections of heart tubes were obtained to determine average cardiac thickness, as previously described (Kronert *et al.*, 2018). For each measurement, a rectangular area of the cardiomyocyte tissue of 10 µm in length and spanning the distance from the inner to outer cardiac cell membrane was highlighted using Adobe Photoshop. The image was imported into National Institutes of Health ImageJ to calculate the area of the highlighted region. The resulting area was divided by 10 µm to yield the average cardiomyocyte thickness for that highlighted region. Cardiomyocyte thickness measurements from dorsal-side or ventral-side images were averaged among biological replicates.

ACKNOWLEDGMENTS

This research was supported by National Institutes of Health (NIH) Grants F31HL128118 to A.S.T., R37GM032443 to S.I.B., and R01HL124091 to A. C. A.S.T. was also supported by a Rees-Stealy Research Foundation Phillips Gausewitz, M.D. Scholar of the San Diego State University (SDSU) Heart Institute Fellowship, a SDSU Graduate Fellowship, and a scholarship from the Achievement Rewards for College Scientists (ARCS) San Diego Chapter. We thank James Caldwell (SDSU) for providing the wild-type 6HisIFI plasmid and the wild-type 6HisIFI fly line. James Caldwell also provided procedures and guidance for purifying the myosin motor domain in bulk from His-tagged flies. We are grateful to Beejal Mehta for providing a Python-based script to measure inter–thick filament distances. We thank Tom Huxford (SDSU) for providing insights on myosin structure and biochemical assays. We also thank the following individuals from SDSU for their technical assistance: Yusur AL-Qaraghuli performed analyses of cardiac physiology data. Julia Platter and Hassler Rengifo performed fly line validation experiments. Additionally, Y. AL-Qaraghuli and H. Rengifo assisted with fly husbandry and performed skeletal muscle functional tests. Jennifer A. Suggs and Floyd Sarsoza provided assistance in IFM microdissections for ATPase assays. William A. Kronert provided assistance in molecular cloning experiments. We acknowledge the use of the SDSU EM Facility and thank Ingrid Niesman and Steven Barlow for their technical assistance for electron microscopy ultrastructure work. X-ray diffraction studies used resources of the Advanced Photon Source, a U. S. Department of Energy (DOE) Office of Science User Facility operated for the DOE Office of Science by Argonne National Laboratory under Contract No. DE-AC02-06CH11357. The BioCAT beamline is supported by Grant P41 GM103622 from the National Institute of General Medical Sciences of the NIH. The content is solely the responsibility of the authors and does not necessarily represent the official views of the NIH.

REFERENCES

Achal M, Trujillo AS, Melkani GC, Farman GP, Ocorr K, Viswanathan MC, Kaushik G, Newhard CS, Glasheen BM, Melkani A, *et al.* (2016). A restrictive cardiomyopathy mutation in an invariant proline at the myosin head/rod junction enhances head flexibility and function, yielding muscle defects in *Drosophila*. J Mol Biol 428, 2446–2461.

Aksel T, Choe Yu E, Sutton S, Ruppel KM, Spudich JA (2015). Ensemble force changes that result from human cardiac myosin mutations and a small-molecule effector. Cell Rep 11, 910–920.

Alsulami K, Marston S (2020). Small molecules acting on myofilaments as treatments for heart and skeletal muscle diseases. Int J Mol Sci 21, 9599.

Bernstein SI, Mogami K, Donady JJ, Emerson CP Jr. (1983). *Drosophila* muscle myosin heavy chain encoded by a single gene in a cluster of muscle mutations. Nature 302, 393–397.
Bernstein SI, O'Donnell PT, Cripps RM (1993). Molecular genetic analysis of muscle development, structure, and function in *Drosophila*. Int Rev Cytol 143, 63–152.
Bhide S, Trujillo AS, O'Connor MT, Young GH, Cryderman DE, Chandran S, Nikravesh M, Wallrath LL, Melkani GC (2018). Increasing autophagy and blocking Nrf2 suppress laminopathy-induced age-dependent cardiac dysfunction and shortened lifespan. Aging Cell 17, e12747.
Bier E, Bodmer R (2004). *Drosophila*, an emerging model for cardiac disease. Gene 342, 1–11.
Bischof J, Maeda RK, Hediger M, Karch F, Basler K (2007). An optimized transgenesis system for *Drosophila* using germ-line-specific phiC31 integrases. Proc Natl Acad Sci USA 104, 3312–3317.
Bloemink MJ, Melkani GC, Dambacher CM, Bernstein SI, Geeves MA (2011). Two *Drosophila* myosin transducer mutants with distinct cardiomyopathies have divergent ADP and actin affinities. J Biol Chem 286, 28435–28443.
Caldwell JT, Melkani GC, Huxford T, Bernstein SI (2012). Transgenic expression and purification of myosin isoforms using the *Drosophila melanogaster* indirect flight muscle system. Methods 56, 25–32.
Cammarato A, Dambacher CM, Knowles AF, Kronert WA, Bodmer R, Ocorr K, Bernstein SI (2008). Myosin transducer mutations differentially affect motor function, myofibril structure, and the performance of skeletal and cardiac muscles. Mol Biol Cell 19, 553–562.
Carlson KA, Gardner K, Pashaj A, Carlson DJ, Yu F, Eudy JD, Zhang C, Harshman LG (2015). Genome-wide gene expression in relation to age in large laboratory cohorts of *Drosophila melanogaster*. Genet Res Int 2015, 835624.
Collier VL, Kronert WA, O'Donnell PT, Edwards KA, Bernstein SI (1990). Alternative myosin hinge regions are utilized in a tissue-specific fashion that correlates with muscle contraction speed. Genes Dev 4, 885–895.
Das N, Levine RL, Orr WC, Sohal RS (2001). Selectivity of protein oxidative damage during aging in *Drosophila melanogaster*. Biochem J 360, 209–216.
Debold EP, Schmitt JP, Patlak JB, Beck SE, Moore JR, Seidman JG, Seidman C, Warshaw DM (2007). Hypertrophic and dilated cardiomyopathy mutations differentially affect the molecular force generation of mouse alpha-cardiac myosin in the laser trap assay. Am J Physiol Heart Circ Physiol 293, H284–H291.
Dickinson MH, Hyatt CJ, Lehmann FO, Moore JR, Reedy MC, Simcox A, Tohtong R, Vigoreaux JO, Yamashita H, Maughan DW (1997). Phosphorylation-dependent power output of transgenic flies: an integrated study. Biophys J 73, 3122–3134.
Dose AC, Ananthanarayanan S, Moore JE, Burnside B, Yengo CM (2007). Kinetic mechanism of human myosin IIIA. J Biol Chem 282, 216–231.
Drummond DR, Hennessey ES, Sparrow JC (1991). Characterisation of missense mutations in the *Act88F* gene of *Drosophila melanogaster*. Mol Gen Genet 226, 70–80.
Fischetti R, Stepanov S, Rosenbaum G, Barrea R, Black E, Gore D, Heurich R, Kondrashkina E, Kropf AJ, Wang S, *et al.* (2004). The BioCAT undulator beamline 18ID: a facility for biological non-crystalline diffraction and X-ray absorption spectroscopy at the Advanced Photon Source. J Synchrotron Radiat 11, 399–405.
Fleming JE, Quattrocki E, Latter G, Miquel J, Marcuson R, Zuckerkandl E, Bensch KG (1986). Age-dependent changes in proteins of *Drosophila melanogaster*. Science 231, 1157–1159.
Holmes KC, Schroder RR, Sweeney HL, Houdusse A (2004). The structure of the rigor complex and its implications for the power stroke. Philos Trans R Soc Lond B Biol Sci 359, 1819–1828.
Houdusse A, Sweeney HL (2016). How myosin generates force on actin filaments. Trends Biochem Sci 41, 989–997.
Irving TC, Maughan DW (2000). *In vivo* x-ray diffraction of indirect flight muscle from *Drosophila melanogaster*. Biophys J 78, 2511–2515.
Kamisago M, Sharma SD, DePalma SR, Solomon S, Sharma P, McDonough B, Smoot L, Mullen MP, Woolf PK, Wigle ED, *et al.* (2000). Mutations in sarcomere protein genes as a cause of dilated cardiomyopathy. N Engl J Med 343, 1688–1696.
Kaushik G, Spenlehauer A, Sessions AO, Trujillo AS, Fuhrmann A, Fu Z, Venkatraman V, Pohl D, Tuler J, Wang M, *et al.* (2015). Vinculin network-mediated cytoskeletal remodeling regulates contractile function in the aging heart. Sci Transl Med 7, 292ra299.
Kawai M, Brandt PW (1980). Sinusoidal analysis: a high resolution method for correlating biochemical reactions with physiological processes in activated skeletal muscles of rabbit, frog and crayfish. J Muscle Res Cell Motil 1, 279–303.
Kawai M, Halvorson HR (1989). Role of MgATP and MgADP in the cross-bridge kinetics in chemically skinned rabbit psoas fibers. Study of a fast exponential process (C). Biophys J 55, 595–603.
Kawai M, Halvorson HR (1991). Two step mechanism of phosphate release and the mechanism of force generation in chemically skinned fibers of rabbit psoas muscle. Biophys J 59, 329–342.
Koppole S, Smith JC, Fischer S (2007). The structural coupling between ATPase activation and recovery stroke in the myosin II motor. Structure 15, 825–837.
Kronert WA, Bell KM, Viswanathan MC, Melkani GC, Trujillo AS, Huang A, Melkani A, Cammarato A, Swank DM, Bernstein SI (2018). Prolonged cross-bridge binding triggers muscle dysfunction in a *Drosophila* model of myosin-based hypertrophic cardiomyopathy. eLife 7, e38064.
Lakdawala NK, Thune JJ, Colan SD, Cirino AL, Farrohi F, Rivero J, McDonough B, Sparks E, Orav EJ, Seidman JG, *et al.* (2012). Subtle abnormalities in contractile function are an early manifestation of sarcomere mutations in dilated cardiomyopathy. Circ Cardiovasc Genet 5, 503–510.
Landis GN, Abdueva D, Skvortsov D, Yang J, Rabin BE, Carrick J, Tavare S, Tower J (2004). Similar gene expression patterns characterize aging and oxidative stress in *Drosophila melanogaster*. Proc Natl Acad Sci USA 101, 7663–7668.
Linari M, Brunello E, Reconditi M, Fusi L, Caremani M, Narayanan T, Piazzesi G, Lombardi V, Irving M (2015). Force generation by skeletal muscle is controlled by mechanosensing in myosin filaments. Nature 528, 276–279.
Lorenz M, Holmes KC (2010). The actin-myosin interface. Proc Natl Acad Sci USA 107, 12529–12534.
McNally EM, Golbus JR, Puckelwartz MJ (2013). Genetic mutations and mechanisms in dilated cardiomyopathy. J Clin Invest 123, 19–26.
McNamara JW, Li A, Dos Remedios CG, Cooke R (2015). The role of super-relaxed myosin in skeletal and cardiac muscle. Biophys Rev 7, 5–14.
Melkani GC, Trujillo AS, Ramos R, Bodmer R, Bernstein SI, Ocorr K (2013). Huntington's disease induced cardiac amyloidosis is reversed by modulating protein folding and oxidative stress pathways in the *Drosophila* heart. PLoS Genet 9, e1004024.
Miller BM, Nyitrai M, Bernstein SI, Geeves MA (2003). Kinetic analysis of *Drosophila* muscle myosin isoforms suggests a novel mode of mechanochemical coupling. J Biol Chem 278, 50293–50300.
Miller MS, Lekkas P, Braddock JM, Farman GP, Ballif BA, Irving TC, Maughan DW, Vigoreaux JO (2008). Aging enhances indirect flight muscle fiber performance yet decreases flight ability in *Drosophila*. Biophys J 95, 2391–2401.
Mulieri LA, Barnes W, Leavitt BJ, Ittleman FP, LeWinter MM, Alpert NR, Maughan DW (2002). Alterations of myocardial dynamic stiffness implicating abnormal crossbridge function in human mitral regurgitation heart failure. Circ Res 90, 66–72.
Muretta JM, Petersen KJ, Thomas DD (2013). Direct real-time detection of the actin-activated power stroke within the myosin catalytic domain. Proc Natl Acad Sci USA 110, 7211–7216.
Nishimura M, Ocorr K, Bodmer R, Cartry J (2011). *Drosophila* as a model to study cardiac aging. Exp Gerontol 46, 326–330.
Ocorr K, Perrin L, Lim HY, Qian L, Wu X, Bodmer R (2007). Genetic control of heart function and aging in *Drosophila*. Trends Cardiovasc Med 17, 177–182.
Ocorr K, Vogler G, Bodmer R (2014). Methods to assess *Drosophila* heart development, function and aging. Methods 68, 265–272.
O'Donnell PT, Bernstein SI (1988). Molecular and ultrastructural defects in a *Drosophila* myosin heavy chain mutant: differential effects on muscle function produced by similar thick filament abnormalities. J Cell Biol 107, 2601–2612.
Onishi H, Mikhailenko SV, Morales MF (2006). Toward understanding actin activation of myosin ATPase: the role of myosin surface loops. Proc Natl Acad Sci USA 103, 6136–6141.
Palmer BM (2010). A strain-dependency of myosin off-rate must be sensitive to frequency to predict the B-process of sinusoidal analysis. Adv Exp Med Biol 682, 57–75.
Palmer BM, Schmitt JP, Seidman CE, Seidman JG, Wang Y, Bell SP, Lewinter MM, Maughan DW (2013). Elevated rates of force development and MgATP binding in F764L and S532P myosin mutations causing dilated cardiomyopathy. J Mol Cell Cardiol 57, 23–31.
Palmer BM, Suzuki T, Wang Y, Barnes WD, Miller MS, Maughan DW (2007). Two-state model of acto-myosin attachment-detachment predicts C-process of sinusoidal analysis. Biophys J 93, 760–769.

Price MG, Landsverk ML, Barral JM, Epstein HF (2002). Two mammalian UNC-45 isoforms are related to distinct cytoskeletal and muscle-specific functions. J Cell Sci 115, 4013–4023.
Rayment I, Rypniewski WR, Schmidt-Base K, Smith R, Tomchick DR, Benning MM, Winkelmann DA, Wesenberg G, Holden HM (1993). Three-dimensional structure of myosin subfragment-1: a molecular motor. Science 261, 50–58.
Richard P, Villard E, Charron P, Isnard R (2006). The genetic bases of cardiomyopathies. J Am Coll Cardiol 48, A79–A89.
Rotstein B, Paululat A (2016). On the morphology of the *Drosophila* heart. J Cardiovasc Dev Dis 3, 15.
Rozek CE, Davidson N (1983). *Drosophila* has one myosin heavy-chain gene with three developmentally regulated transcripts. Cell 32, 23–34.
Schmitt JP, Debold EP, Ahmad F, Armstrong A, Frederico A, Conner DA, Mende U, Lohse MJ, Warshaw D, Seidman CE, Seidman JG (2006). Cardiac myosin missense mutations cause dilated cardiomyopathy in mouse models and depress molecular motor function. Proc Natl Acad Sci USA 103, 14525–14530.
Seidman JG, Seidman C (2001). The genetic basis for cardiomyopathy: from mutation identification to mechanistic paradigms. Cell 104, 557–567.
Spudich JA (2014). Hypertrophic and dilated cardiomyopathy: four decades of basic research on muscle lead to potential therapeutic approaches to these devastating genetic diseases. Biophys J 106, 1236–1249.
Suggs JA, Cammarato A, Kronert WA, Nikkhoy M, Dambacher CM, Megighian A, Bernstein SI (2007). Alternative S2 hinge regions of the myosin rod differentially affect muscle function, myofibril dimensions and myosin tail length. J Mol Biol 367, 1312–1329.
Swank DM (2012). Mechanical analysis of *Drosophila* indirect flight and jump muscles. Methods 56, 69–77.
Swank DM, Bartoo ML, Knowles AF, Iliffe C, Bernstein SI, Molloy JE, Sparrow JC (2001). Alternative exon-encoded regions of *Drosophila* myosin heavy chain modulate ATPase rates and actin sliding velocity. J Biol Chem 276, 15117–15124.
Swank DM, Vishnudas VK, Maughan DW (2006). An exceptionally fast actomyosin reaction powers insect flight muscle. Proc Natl Acad Sci USA 103, 17543–17547.
Swank DM, Wells L, Kronert WA, Morrill GE, Bernstein SI (2000). Determining structure/function relationships for sarcomeric myosin heavy chain by genetic and transgenic manipulation of *Drosophila*. Microsc Res Tech 50, 430–442.
Taft MH, Behrmann E, Munske-Weidemann LC, Thiel C, Raunser S, Manstein DJ (2013). Functional characterization of human myosin-18A and its interaction with F-actin and GOLPH3. J Biol Chem 288, 30029–30041.
Thummel C, Pirrotta V (1992). Technical notes: new pCasper P-element vectors. Drosoph Inf Serv 71, 150.
Ujfalusi Z, Vera CD, Mijailovich SM, Svicevic M, Yu EC, Kawana M, Ruppel KM, Spudich JA, Geeves MA, Leinwand LA (2018). Dilated cardiomyopathy myosin mutants have reduced force-generating capacity. J Biol Chem 293, 9017–9029.
Villard E, Duboscq-Bidot L, Charron P, Benaiche A, Conraads V, Sylvius N, Komajda M (2005). Mutation screening in dilated cardiomyopathy: prominent role of the beta myosin heavy chain gene. Eur Heart J 26, 794–803.
Viswanathan MC, Tham RC, Kronert WA, Sarsoza F, Trujillo AS, Cammarato A, Bernstein SI (2017). Myosin storage myopathy mutations yield defective myosin filament assembly *in vitro* and disrupted myofibrillar structure and function *in vivo*. Hum Mol Genet 26, 4799–4813.
Zahn JM, Sonu R, Vogel H, Crane E, Mazan-Mamczarz K, Rabkin R, Davis RW, Becker KG, Owen AB, Kim SK (2006). Transcriptional profiling of aging in human muscle reveals a common aging signature. PLoS Genet 2, e115.
Zoghbi ME, Woodhead JL, Moss RL, Craig R (2008). Three-dimensional structure of vertebrate cardiac muscle myosin filaments. Proc Natl Acad Sci USA 105, 2386–2390.